HHS Public Access

Author manuscript

Neuron. Author manuscript; available in PMC 2023 May 04.

Published in final edited form as:

Neuron. 2022 May 04; 110(9): 1532–1546.e4. doi:10.1016/j.neuron.2022.01.025.

Differential dendritic integration of long-range inputs in association cortex via subcellular changes in synaptic AMPA-to-NMDA receptor ratio

Mathieu Lafourcade[1], **Marie-Sophie H. van der Goes**[1], **Dimitra Vardalaki**[1], **Norma J. Brown**[1], **Jakob Voigts**[1], **Dae Hee Yun**[2], **Minyoung E. Kim**[2], **Taeyun Ku**[2], **Mark T. Harnett**[1,*]

[1]McGovern Institute for Brain Research, Department of Brain & Cognitive Sciences, Massachusetts Institute of Technology, Cambridge, MA, 02139, USA

[2]Picower Institute for Learning & Memory, Department of Brain & Cognitive Sciences, Massachusetts Institute of Technology, Cambridge, MA, 02139, USA

Summary

Synaptic NMDA receptors can produce powerful dendritic supralinearities that expand the computational repertoire of single neurons and their respective circuits. This form of supralinearity may represent a general principle for synaptic integration in thin dendrites. However, individual cortical neurons receive many diverse classes of input that may require distinct postsynaptic decoding schemes. Here, we show that sensory, motor, and thalamic inputs preferentially target basal, apical oblique, and distal tuft dendrites, respectively, in layer 5b pyramidal neurons of mouse retrosplenial cortex, a visuo-spatial association area. These dendritic compartments exhibited differential expression of NMDA receptor-mediated supralinearity due to systematic changes in AMPA-to-NMDA receptor ratio. Our results reveal a new schema for integration in cortical pyramidal neurons, in which dendrite-specific changes in synaptic receptors support input-localized decoding. This coexistence of multiple modes of dendritic integration in single neurons has important implications for synaptic plasticity and cortical computation.

eTOC Blurb

Lafourcade et al. reveal that apical oblique dendrites of retrosplenial cortical L5 neurons exhibit unexpectedly linear integration compared to basal and tuft branches, via increased synaptic

*Corresponding author and lead contact: harnett@mit.edu.

Author Contributions

M.L. performed sCRACM and uncaging, analyzed data, and made figures. M.S.H.v.d.G performed preliminary sCRACM and anatomy experiments, data analysis, and helped write the manuscript. D.V. performed synaptic stimulation experiments, a subset of uncaging experiments, analyzed the respective data, and made the corresponding figures. N.J.B. performed monosynaptic rabies tracing and anterograde axon labeling experiments and analyzed the data. J.V. helped with axonal anatomy data analysis. M.E.K, T.K., & D.H.Y. performed preliminary anatomy experiments. M.T.H supervised all aspects of the project and wrote the manuscript.

Declaration of interests

The authors declare no competing interests.

AMPA:NMDA. Long-range inputs are targeted to these distinct dendritic domains, supporting the idea that single neurons perform a diverse range of subcellular processing.

Keywords

Dendritic Integration; Retrosplenial Cortex; AMPA:NMDA; Layer 5 Pyramidal Cells; sCRACM

Introduction

Decades of theoretical and biophysical studies have shown that dendrites strongly influence input-output transformations, endowing single neurons with substantial computational capabilities (Poirazi, Brannon and Mel, 2003; Polsky, Mel and Schiller, 2004; London and Häusser, 2005; Larkum, Nevian, Sandler, Polsky, Schiller, 2009; Branco, Clark, Häusser, 2010; Major, Larkum and Schiller, 2013). This is implemented via subcellular distribution of active and passive conductances, which control neuronal activity both at the local and global level (Markram, Helm and Sakmann, 1995; Andrásfalvy and Magee, 2001; Migliore and Shepherd, 2002; Harnett *et al.*, 2013; Harnett, Magee and Williams, 2015). Active dendritic processing of different spatiotemporal input patterns has been shown to contribute to both moment-to-moment computation and learning-related plasticity in the mammalian brain (Losonczy, Makara and Magee, 2008; Xu *et al.*, 2012; Larkum, 2013; Gambino *et al.*, 2014; Bittner *et al.*, 2015, 2017; Ranganathan *et al.*, 2018). However, it is unknown how different postsynaptic integration mechanisms are organized in dendrites with respect to their anatomical input streams. Long-range corticocortical, corticothalamic, and local inputs may be targeted to specific dendritic domains and may exhibit distinct statistical structure, requiring specific decoding. Addressing this issue is key to understanding how single neurons, and their respective circuits, process information.

One of the first studies to propose a model of compartmentalized dendritic computation identified nonlinear sigmoidal events produced by the synchronous activation of spatially clustered inputs via the NMDA receptor (NMDAR) (Mel, 1991). Such “NMDA spikes” have subsequently been observed in several classes of mammalian central neurons (Mel, 1991; Schiller *et al.*, 2000; Nevian *et al.*, 2007; Major *et al.*, 2008; Katona *et al.*, 2011; Krueppel, Remy and Beck, 2011; Plotkin, Day and Surmeier, 2011; Brandalise *et al.*, 2016). These nonlinearities are specifically expressed in thin branches (Schiller *et al.*, 2000; Schiller and Schiller, 2001; Polsky, Mel and Schiller, 2004; Nevian *et al.*, 2007; Losonczy, Makara and Magee, 2008; Branco and Häusser, 2011; Major, Larkum and Schiller, 2013) and have been shown to play a role in increasing neuronal responses and selectivity in cortical pyramidal cells (PCs) (Lavzin *et al.*, 2012; Gambino *et al.*, 2014; Palmer *et al.*, 2014). NMDA spikes have further been proposed as a universal principle for synaptic integration in thin dendrites (Larkum, Nevian, Sandler, Polsky and Schiller, 2009; Major, Larkum and Schiller, 2013). However, this has not been thoroughly explored. Furthermore, the identity of the relevant inputs in previous NMDAR nonlinearity experiments is largely unknown. Recent evidence suggests that synaptic inputs with similar tuning properties are clustered (Iacaruso, Gasler and Hofer, 2017; Scholl, Wilson and Fitzpatrick, 2017; Ju *et al.*, 2020) and that long-range inputs can be highly spatially organized (Zhang *et al.*, 2016; Yamawaki *et al.*,

2019). Thus, local thin dendrite operations may be specialized for processing the particular statistics of certain inputs. No studies have evaluated this possible role for different dendritic compartments as unique intersections of diverse biophysical properties and synaptic inputs in regulating single cell firing output.

The diversity of inputs and complex receptive fields of PCs in associative areas makes them compelling candidates to investigate how different channels of subcellular input are processed across the dendritic arbor. Association cortices integrate inputs from diverse modalities to produce complex high-dimensional representations that guide behavior (Harvey, Coen and Tank, 2012; Mante *et al.*, 2013; Rigotti *et al.*, 2013). This is reflected even at the level of individual neurons across species (Mante *et al.*, 2013; Rigotti *et al.*, 2013; Alexander and Nitz, 2015; Sarafyazd and Jazayeri, 2019). While dendritic integration in associative areas remains poorly studied compared to sensory areas, ex vivo experiments in rat prefrontal cortex (PFC) have demonstrated that some of the basic biophysical mechanisms are conserved (Kalmbach *et al.*, 2013; Dembrow, Zemelman and Johnston, 2015). Additionally, two recent studies found evidence for engagement of active dendritic processing in awake mouse PFC (Labarrera *et al.*, 2018) and retrosplenial cortex (RSC) (Voigts and Harnett, 2020). These studies all focused on interactions between the soma and the apical trunk dendrite, not on integration in thin branches, where most synapses are made.

RSC is a compelling model associative area to test how different dendritic domains process distinct input streams. RSC has dense interconnections with multiple thalamic nuclei, hippocampal, and parahippocampal regions, as well as motor and visual cortices (Wyss and Vangroen, 1992; Shibata, 1993; Van Groen and Wyss, 2003; Sugar *et al.*, 2011), consistent with its role in spatial memory and navigation (Vann, Aggleton and Maguire, 2009; Knight and Hayman, 2014; Miller *et al.*, 2014; Mitchell *et al.*, 2018; Fischer *et al.*, 2019). Despite extensive work on RSC anatomy, little is known about the functional organization of long-range connectivity to specific cell types in this region (Yamawaki *et al.*, 2019), as is the case for almost all associate cortices. We combined circuit and cellular approaches to map the spatial distribution of functional long-range inputs onto the dendritic arbor of L5b PCs in mouse RSC. We focused on L5b PCs (also called thick-tufted or Extra-Telencephalic neurons) because they have the most extensive dendritic arbor among cortical neurons, spanning layers 1–6, and they provide the major subcortical output throughout the cortex (Kim *et al.*, 2015). We next tested the integrative properties of different L5b PC dendritic domains in the context of the functional spatial mapping results. Finally, we identified a new synaptic mechanism supporting distinct integration modes in particular dendritic compartments.

Results

Input-specific subcellular connectivity rules for L5b pyramidal neurons in RSC.

The emergence of diverse visuo-spatial receptive fields associated with vision, self-motion, and heading (Cho and Sharp, 2001; Alexander and Nitz, 2015; Jacob *et al.*, 2017; Fischer *et al.*, 2019; Alexander *et al.*, 2020) suggests that RSC A30 (the more dorsal, dysgranular subdivision) receives inputs from visual and motor cortices as well as thalamic areas (Wyss and Vangroen, 1992; Shibata, 1993; Van Groen and Wyss, 2003; Sugar *et al.*, 2011). To

identify areas that provide direct inputs to RSC A30 in mice, we performed monosynaptic rabies tracing (Wickersham and Sullivan, 2015) in C57/BL6 mice (Fig. 1). Our data show substantial long-range inputs to A30 from ipsilateral primary visual cortex (V1), secondary motor cortex (M2), and lateral dorsal thalamus (LD), consistent with classical anatomical studies in rats showing that RSC A30 receives inputs from multiple discrete cortical and subcortical regions (Wyss and Vangroen, 1992; Shibata, 1993; Van Groen and Wyss, 2003; Sugar *et al.*, 2011). As a control, we observed little to no input from a region previously shown not to project to RSC: primary somatosensory cortex ($p<0.05$ for S1 versus V1, M2, & LD; Mann Whitney, n=5 mice, all ipsilateral comparisons). While we did observe other inputs to A30 including A29 RSC (the medial, granular subdivision), anterior cingulate cortex, primary motor cortex, and other thalamic areas, we focused on V1, M2, and LD as key inputs for RSC's role in visuospatial navigation. Although our monosynaptic rabies tracing was performed with synapsin and CamKII promoters in wild-type mice, our injections mostly infected L5 neurons (Fig. 1A & Supplementary Fig. S1).

To assess how V1, M2, and LD inputs were organized at the level of single neurons, we used Subcellular Channelrhodopsin Assisted Circuit Mapping (SCRACM) (Petreanu *et al.*, 2009) to reveal the functional synaptic density of a specified input across the dendritic arbor of individual neurons. We first targeted ChR2-expressing AAV injections to V1 in adult mice (Fig. 2A & Supplementary Fig. S2). After 4 weeks of ChR2 expression, we performed patch clamp recording of L5b PCs in acute slices of RSC that contained ChR2-infected axons from V1 (Supplementary Fig. S3). We activated ChR2 in V1 axons using a grid of ~50 μm diameter spots of 473 nm laser light, sequentially delivered across the dendritic arbor of the recorded neuron in the presence of TTX to block axonal conduction (Fig. 2B). We observed EPSPs when the laser spot was near the soma, as opposed to the apical trunk dendrite or tuft (Fig. 2C&D), indicating that V1 axon terminals preferentially made functional synapses at the basal and proximal oblique dendrites of L5b PCs in RSC A30. All neurons receiving direct V1 input (16 neurons from 11 mice) displayed a similar perisomatic connectivity pattern (Fig. 2E). Different patterns were observed for M2 and LD inputs (Fig. 2F–O). M2 axons preferentially made functional synapses at the proximal trunk and oblique dendrites (n=18 neurons from 13 mice), while LD axons made the vast majority of their synaptic contacts in the distal apical dendritic tuft (n=7 neurons from 5 mice; two-way ANOVA: p=0.0228 input source, p=2.77e–06 distance from pia, p=2.03e–30 input source*distance from pia; see Fig. S3 for laminar profiles used for statistical analyses).

Does the functional organization of synaptic inputs to L5b neurons in RSC A30 simply reflect the laminar distribution of axonal fibers from the different regions (i.e. does it follow Peters' rule (Rees, Moradi and Ascoli, 2017))? To address this, we quantified the axonal fiber density in RSC A30 from cells in V1, M2, and LD that expressed tdTomato or mCherry (Supplementary Fig. S3). We observed a substantial discrepancy between laminar fiber density and functional connectivity on L5b cells (Supplementary Fig. S3B&C). Despite no functional connectivity in the tuft dendrites of L5b cells, V1 and M2 axons ramify in layer 1 (L1), suggesting they make numerous synapses at other cell types. Additionally, LD axons display two narrow, dense bands of fibers in L1 and L3. However, only the band in L1 appears to form synapses on L5b cells in RSC A30. This is in contrast to a recent report in which anterior thalamic axons project specifically to L1 of RSC A29 and

form most of their synapses onto L5 neurons in this zone (Yamawaki *et al.*, 2019). Our results instead provide further evidence that, in general, axo-dendritic anatomical overlap is not an accurate predictor of functional synaptic connections. Instead, a highly selective connectivity program seems to control the functional architecture of long-range excitatory inputs to L5b PCs.

Distinct postsynaptic integration modes in different L5b PC dendritic domains.

We next asked whether the organization of V1, M2, and LD inputs to particular dendritic zones was associated with differences in synaptic integration. We combined somatic patch clamp recording with two-photon imaging and rapid multi-site two-photon glutamate uncaging at the different classes of dendritic branches corresponding to V1, M2, and LD inputs: basals, apical obliques, and distal apical tufts, respectively. We measured the summation of uncaging-evoked excitatory postsynaptic potentials (uEPSPs) at 20 to 40 spines distributed along ~20–50 μm of a single branch. We compared "expected" uEPSPs (the arithmetic sum of individual spine uEPSPs) to the "measured" uEPSP (when the same group of spines was quasi-simultaneously activated with a 0.12 ms inter-stimulus interval (isi)).

Basal branches exhibited a dramatic increase in measured versus expected uEPSPs after ~10–20 inputs, or ~4–8 mV somatic depolarization (Fig. 3, n=19 branches from 14 neurons from 12 mice). This supralinear summation was always accompanied by a large calcium signal in the dendritic branch, as measured with OGB-6F; Fig. 3B,D,F). To normalize for different local dendritic impedances across experiments, we aligned all examined branches to a threshold calcium signal (50% ΔF/F) and plotted gain as the ratio between measured and expected uEPSPs (Fig. 3E). Basal branches displayed a high uEPSP gain (2.61±0.23) due to supralinear summation. All basal branches tested displayed a large local branch calcium signal well before an action potential (AP) could be initiated at the soma/axon (Fig. 3F; 1.29±0.11 ΔF/F). The shape of supralinear uEPSPs and corresponding OGB-6F signals resembled previously described NMDAR-mediated supralinearity ("NMDA spikes") (Schiller *et al.*, 2000; Nevian *et al.*, 2007). We therefore bath-applied the NMDAR antagonists MK-801 and D-AP5 (Fig. 3E–F), which linearized the gain (2.11±0.14 control gain versus 1.03±0.06 after NMDAR antagonist application, n=3 neurons, p=0.0156, Wilcoxon-Signed Rank test) and substantially reduced the associated branch Ca^{2+} signal (1.75±0.29 control ΔF/F after threshold versus 0.25±0.04 after NMDAR antagonist application, n=3 neurons, p=0.0156, Wilcoxon Signed-Rank test). Additional unpaired experiments were performed with NMDAR antagonists already present in the bath (Supplementary Fig. S4), all of which showed linear gain (1.11±0.09) and reduced branch Ca^{2+} signals (0.18±0.02) compared to the control population (n=16 branches, p<0.0001 for both gain and calcium signal, Mann-Whitney). These experiments demonstrated the presence of a robust NMDAR-mediated supralinear summation mechanism in associative cortex, specifically in the basal dendrites of L5b neurons in RSC A30, similar to that described in sensory cortex PCs (Nevian *et al.*, 2007; Branco, Clark and Häusser, 2010; Major, Larkum and Schiller, 2013).

We next examined integration in distal tuft dendrites (Fig. 4), which, in RSC A30 L5b cells, receive LD inputs in L1 (Fig. 2K–O). We performed uncaging experiments as detailed above, but grouped 3 to 5 spines together for unitary events in order to overcome distance-dependent electrotonic filtering from the tuft to the soma (Stuart and Spruston, 1998; Harnett *et al.*, 2013; Harnett, Magee and Williams, 2015). Tuft dendrites in mouse RSC A30 L5b PCs exhibited supralinear integration (gain:1.63±0.10; calcium signal: 1.02±0.12 ΔF/F), which was NMDA-dependent (gain:0.97±0.05, calcium signal: 0.36±0.07 ΔF/F after bath application of MK-801 and D-AP5, p=0.0078 and p=0.0313, Wilcoxon Signed-Rank test for gain and Ca^{2+}, respectively), consistent with previous reports from the primary somatosensory cortex of rats (Larkum, Zhu and Sakmann, 1999; Larkum, Nevian, Sandler, Polsky and Schiller, 2009). The amplitude of threshold uEPSPs in tuft branches was smaller than in basal branches (4.8±0.4 mV for n=16 tuft branches versus 8.1±0.6 mV for n=21 basal branches, p<0.0001, Mann-Whitney), congruent with their remote electrotonic location. Interestingly, the magnitude of tuft supralinearity was more modest and the gain curve was biphasic (Fig. 4E), despite increasing Ca^{2+} signals (Fig. 4F). This indicates that tuft branches have distinct integration mechanisms compared to basal branches, due to distinct synaptic properties, ion channel distributions, and/or electrotonic location from the axon (Harnett *et al.*, 2013; Harnett, Magee and Williams, 2015).

NMDAR-mediated supralinearity is thought to represent a general principle for how thin spiny dendrites integrate excitatory input (Mel, 1991; Schiller *et al.*, 2000; Poirazi, Brannon and Mel, 2003; Branco, Clark, and Häusser, 2010; Branco and Häusser, 2011; Larkum, 2013; Major, Larkum and Schiller, 2013). Though both basal and tuft branches in RSC A30 L5 PCs showed supralinear integration, they exhibited divergent features. We therefore tested the thin dendrites located between tufts and basals along the longitudinal axis of the neuron, the proximal oblique branches. Surprisingly, we observed a different input-output function in oblique versus basal and tuft dendrites (Fig. 5), even within the same cell (Supplementary Fig. S5). Oblique branches were largely linear (maximum gain prior to AP initiation:1.23±0.03, n=45 branches from 36 neurons; p=9.56e–10 for basal vs oblique, p=3.26e–9 for tuft versus oblique, Tukey-Kramer multiple comparisons after one-way ANOVA correction), with minimal local Ca^{2+} signals (0.23±0.01 ΔF/F), even as we increased input number to trigger conventional axosomatic APs. In a few cases (6 out of 45), a modest Ca^{2+} signal could be observed just before (~1–3 inputs) AP initiation along with slightly supralinear integration in this narrow window. NMDAR antagonists had almost no effect on integration (gain:1.1±0.05, p=0.14, Mann Whitney) or the pre-AP Ca^{2+} signals (ΔF/F:0.17±0.03, p=0.11, Mann Whitney; n=6 branches from 6 slices; Fig. 5 E,F), in contrast to basal (Fig. 3) and tuft (Fig. 4) dendrites). We additionally performed multi-pulse synaptic stimulation of apical oblique dendrites, as has been used previously to evoke NMDA spikes (Polsky, Mel and Schiller, 2004, 2009; Gordon, Polsky and Schiller, 2006), to complement our uncaging experiments. These experiments also showed linear integration in apical oblique branches (Supplementary Fig. 7). Together, these data demonstrate distinct dendritic integration modes in thin dendrites (and in the same cells).

Subcellular compartment-specific regulation of synaptic AMPA-to-NMDA receptor ratio underlies integration mode differences across the dendritic arbor of RSC A30 L5b PCs

Why were oblique branches so different from basal and tuft dendrites on the same cells? The differences were not due to systematic variation in uncaging location (Supplementary Fig. S6). Linear integration is not a property of spiny dendrites (but see Bathellier, Margrie and Larkum, 2009; Kumar *et al.*, 2018), so our results are in contrast with prior assertions that all spiny dendrites possess NMDAR-mediated supralinearity (Schiller *et al.*, 2000; Schiller and Schiller, 2001; Branco, Clark, and Häusser, 2010; Larkum, 2013; Major, Larkum and Schiller, 2013). Aspiny dendrites of cerebellar interneurons, however, have been shown to lack any supralinear mechanisms, limiting them to only linear or even sublinear integration (Abrahamsson *et al.*, 2012; Tran-Van-Minh *et al.*, 2016). Perhaps oblique branch depolarization triggers a local Na^+ spike which could couple strongly to axonal AP initiation, obscuring a potential supralinearity (Ariav, Polsky and Schiller, 2003; Losonczy, Makara and Magee, 2008; Sivyer and Williams, 2013; Sun *et al.*, 2014). We thus uncoupled oblique dendrites from axosomatic AP initiation by hyperpolarizing the soma with direct current injection (range: 12–18 mV) (Losonczy, Makara and Magee, 2008; Sun *et al.*, 2014). This did not reveal any “hidden” supralinear integration (gain: 0.91±0.04, Fig. 6A–C) or any evidence of dendritic spikelets (Supplementary Fig. S6D), arguing against local branch Na^+ spikes in L5b PC oblique dendrites, in contrast to what has been reported in nonpyramidal cells (Chen, Midtgaard and Shepherd, 1997; Sivyer and Williams, 2013; Gale and Murphy, 2016) as well as CA1 (Ariav, Polsky and Schiller, 2003; Losonczy and Magee, 2006) and CA2 (Sun *et al.*, 2014) pyramidal cells. We additionally tested if local voltage-activated Ca^{2+} channel (VACC) activity could be differentially contributing either directly to supralinear integration in basal branches or indirectly by confounding our Ca^{2+} proxy measurements of local branch depolarization. We evoked bursts of backpropagating APs via somatic current injection and measured the OGB6F signals at various locations along the two branch types (Supplementary Fig. S6). We observed no differences in local Ca^{2+} signals between oblique and basal branches, suggesting no systematic differences in VACCs in these compartments (mean $\Delta F/F$ basals:0.85±0.05, obliques:0.94±0.04, $p=0.10$, Mann-Whitney, n=46 and n=62 respectively).

We then asked if AP initiation was potentially occluding a higher threshold for NMDAR supralinearity. Maybe these branches could express supralinear integration at more depolarized voltages, when the cell would normally be firing. We thus applied TTX (1 μM) to block axonal AP initiation (Fig. 6D–F) and re-evaluated branch integration. This allowed us to observe a modest supralinearity at more depolarized potentials in oblique branches (gain:1.58±0.09, $p=0.0273$, Wilcoxon Signed-Rank versus control, n=16 branches from 16 slices). This was still less than we observed under control conditions in basal branches, but similar to tuft branches under control conditions ($p<0.0001$ and $p=0.3865$, respectively, Mann-Whitney). This suggested that although some NMDARs were indeed present at the synapses on oblique branches, they were insufficient to enable strong supralinear integration under physiological conditions.

The expression of NMDAR-mediated supralinearity should depend on the AMPAR-to-NMDAR ratio (AMPA:NMDA) at the activated synapses: if the ratio is high, AMPAR

conductance would drive the cell to axosomatic AP threshold (or to the synaptic reversal potential) before NMDARs could contribute significant current (Harnett *et al.*, 2012; Tran-Van-Minh *et al.*, 2015; Beaulieu-Laroche and Harnett, 2018). We therefore tested if experimentally decreasing AMPA:NMDA could artificially convert linear integration in oblique dendrites into the supralinear regime. We applied a sub-saturating concentration of the AMPAR antagonist DNQX (2–3 μM) during uncaging, which indeed resulted in the expression of modest oblique branch supralinearity (gain:1.57±0.12, p=0.0023 vs control, Mann-Whitney, n=10 branches, 10 slices, 3 animals; Fig. 6G–I). Similar to TTX application, this oblique branch supralinearity was smaller than that observed in the basals (p=0.0036, Mann Whitney). This suite of pharmacological and physiological experiments suggest that the linear integration in RSC A30 L5b PC oblique dendrites is due to a subcellular biophysical specialization of high AMPA:NMDA specifically at the synapses in these branches.

Changes in AMPA:NMDA have previously been reported to mediate cell-wide synaptic changes in development (Hall and Ghosh, 2008; Zito *et al.*, 2009), plasticity (Kauer, Malenka and Nicoll, 1988; Malinow and Malenka, 2002; Watt *et al.*, 2004), addiction (Ungless *et al.*, 2001; Van Den Oever *et al.*, 2008), and stress (Saal *et al.*, 2003). However, accurate measurement of synaptic AMPA:NMDA in neurons is notoriously difficult due to space clamp confounds (Rall and Segev, 1985; Spruston, Jaffe, Williams, and Johnston, 1993; Williams and Mitchell, 2008; Beaulieu-Laroche and Harnett, 2018). We therefore developed a physiological assay to compare AMPA:NMDA at single synapses using current clamp, which is much less sensitive to space clamp distortion. We first activated individual spines at a given branch with glutamate uncaging under control conditions to produce approximately physiologically-sized unitary uEPSPs (Fig. 7B). We then washed on DNQX and 0 mM Mg^{2+} aCSF and repeated the uncaging at the same spines. This allowed us to create a ratio of mostly AMPAR-mediated uEPSP amplitude to mostly NMDAR-mediated uEPSP amplitude for 66 spines in 6 basal branches versus 64 spines in 6 oblique dendrites (11 neurons from 3 mice). Consistent with Fig. 6, we observed a significant increase in AMPA:NMDA for spines located at oblique dendrites (median=2.69) compared to basals (median=1.84; Fig.7D, p=0.0005, Mann-Whitney U test).

To control for any potential confounds associated with glutamate uncaging, we performed the same experiment using local microstimulation of presynaptic axons with bipolar theta glass electrodes (Polsky, Mel and Schiller, 2004, 2009; Gordon, Polsky and Schiller, 2006; Lavzin *et al.*, 2012) to activate small groups of synapses at basal versus apical oblique branches (Fig. 7C). Results from this experiment produced even more substantial differences in AMPA:NMDA than we observed with uncaging (Fig. 7D; median basal AMPA:NMDA=3.1 vs. median oblique AMPA:NMDA=5.48, Fig. 7D, p=0.009, Mann-Whitney U test).

Together, these data show that subcellular organization of synaptic AMPA:NMDA gives rise to the different dendritic integration modes we observed in basal versus oblique branches of RSC A30 L5b PCs.

Discussion

Our experiments provide new insight into how single cortical neurons in association cortex receive and process their inputs at the subcellular level before final integration at the axon. We discovered distinct, dendritic compartment-specific biophysical mechanisms that give rise to different postsynaptic integration rules within the same cells. The same compartment segregation is reflected in the highly organized, dendrite-preferential synaptic organization of three distinct excitatory long-range inputs. Notably, the distribution of axons from the three input regions to RSC A30 is not predictive of the synaptic connectivity rules (Rees, Moradi and Ascoli, 2017) in L5b cells (Fig. 1 vs. Fig. 2), suggesting cell type-specific mechanisms underlying the wiring logic. This cellular and circuit arrangement is evidence of input-specific integration in cortical PCs, supporting the idea that dendrites act as separate computational units (Polsky, Mel and Schiller, 2004), extracting distinct information and performing unique operations.

We found that basal dendrites of RSC A30 L5b PCs preferentially received V1 input and exhibited highly supralinear integration of spatiotemporally clustered inputs (Fig. 2). In contrast, apical obliques branches, the main targets of M2 input, which could only integrate their inputs linearly (Fig. 4) as a result of a high synaptic AMPA:NMDA (Fig. 7). Apical tuft dendrites, which selectively received thalamic input, showed a modest supralinear integration of spatiotemporally-clustered input (Fig. 3). This functional architecture expands the possible modes of subcellular processing in cortical PCs (Gordon, Polsky and Schiller, 2006; Larkum, Nevian, Thomas, Sandler, Polsky, Schiller, 2009; Major, Larkum and Schiller, 2013) and suggests that a modified, non-uniform two-layered network model for pyramidal neurons (Poirazi, Brannon and Mel, 2003) might better capture RSC L5b PCs computations.

The relationship between dendritic branch integration mode and AP initiation

The degree of supralinearity we observed at oblique branches under TTX treatment (Fig. 6D–F) resembled that of tuft dendrites under control conditions. This suggests that the electrotonic distance of tuft branches from the AP initiation site (i.e. the axon) plays an important role in regulating integration, allowing tuft dendrites to express supralinearity. This is due to the ability of distal tuft branches to depolarize much more than proximal branches without triggering an axonal AP (or a dendritic trunk spike) (Williams and Stuart, 2002; Williams, 2004; Larkum, Nevian, Sandler, Polsky and Schiller, 2009; Beaulieu-Laroche *et al.*, 2018). Conversely, the low AMPA:NMDA in basal dendrites allows even modest local synaptic depolarization from spatiotemporally-clustered input to recruit substantial NMDAR-mediated nonlinearity, below the threshold for axonal AP initiation, despite the relatively short electrotonic distance. Importantly, this mechanism endows basal dendrites with a large window for coincidence detection (Tran-Van-Minh *et al.*, 2015).

Our results show that NMDAR-mediated supralinearity does not generalize to all thin spiny branches, contrary to previous assertions (Schiller *et al.*, 2000; Schiller and Schiller, 2001; Poirazi, Brannon and Mel, 2003; Branco, Clark, Häusser, 2010; Larkum, 2013; Major, Larkum and Schiller, 2013). In fact, oblique dendrites exhibited linear integration, with almost no local Ca^{2+} influx until AP initiation, in response to either glutamate

uncaging (Fig. 5) or synaptic stimulation (Supplementary Fig. S7). Interestingly, radial oblique dendrites of hippocampal CA1 PCs exhibit a supralinearity mediated by fast local Na^+ spikes (Losonczy and Magee, 2006), contrasting with our observations here. Our results indicate that regardless of the number or pattern of inputs to oblique branches, the postsynaptic neuron can only represent linear combinations of this input, in contrast to what has been reported for the various spatio-temporal input-pattern sensitivities of basal branches (Mel, 1991; Poirazi and Mel, 2000; Branco, Clark, and Häusser, 2010; Branco and Häusser, 2011). This insensitivity of oblique dendrites to the spatiotemporal pattern of input could be advantageous for specific forms of processing: for example, potentially graded boosting of back-propagating action potentials (bAPs) along the apical trunk (Stuart, Greg, Häusser, 2001). Additionally, linear integration may also be important for the transformation(s) that RSC L5b neurons perform on M2 inputs: for example, to represent continuous motor variables, such as locomotion or head versus body motion. Future work will be necessary to explore how these different modes of integration interact in the intact cortex during behavior.

Dendritic domain-specific regulation of AMPA:NMDA

While numerous prior studies have investigated AMPA:NMDA as a function of experience (development, learning, stress, drug exposure), few have examined it as a function of input pathway (Kumar and Huguenard, 2003). The vast majority of these studies relied on extracellular stimulation of afferent axons, which is challenging to interpret in cortex (Histed, Bonin and Reid, 2009), as well as whole-cell voltage clamp, which also has serious technical confounds (Rall and Segev, 1985; Spruston, Jaffe, Williams, and Johnston, 1993; Williams and Mitchell, 2008, Beaulieu-Laroche and Harnett, 2018). Our single synapse current-clamp based approach directly showed compartment-specific differences in functional receptor-mediated conductance with previously unachievable level of detail and accuracy. Despite the voltage-dependent nature of Mg^{+2} block, uncaging at single spines does not produce sufficient local depolarization to activate enough NMDAR conductance (Harnett *et al.*, 2012; Beaulieu-Laroche and Harnett, 2018) to contaminate our AMPA uEPSP measurements. The findings support compartment-specific control of AMPA:NMDA that produces the observed differences between dendritic integration rules. It is currently unclear if this represents a general principle of L5 PCs. There is some prior support for the idea that AMPA:NMDA can vary across the dendritic arbor of pyramidal neurons (Andrásfalvy and Magee, 2001): AMPARs, but not NMDARs, were reported to increase at synapses as a function of distance from the soma along the somato-dendritic axis in an electron microscopy study in hippocampal CA1 PCs (Nicholson *et al.*, 2006).

Implications for synaptic plasticity

The striking segregation of inputs we observed may be particularly important for implementing compartment- and/or input-specific plasticity rules and mechanisms. First, segregated inputs are less likely to interact in terms of synaptic plasticity, due to the spatial compartmentalization of electrical and chemical signals (Harvey and Svoboda, 2007), a feature that enables tuning of independent computations. Second, by spatially segregating different inputs in distinct dendritic compartments, single neurons can more easily implement discrete postsynaptic mechanisms for input-specific decoding, for example by taking advantage of differential trafficking of ion channels (Andrásfalvy and Magee,

2001; Migliore and Shepherd, 2002; Harnett *et al.*, 2013; Trimmer, 2015). Third, the specific biophysical mechanisms which underlie differential integration in L5b PCs (changes in AMPA:NMDA and threshold for axonal AP initiation) are likely to directly influence plasticity induction. NMDA spikes produce large local Ca^{2+} signals independent of bAPs, providing a compelling substrate for compartmentalized learning rules (Gordon, Polsky and Schiller, 2006). Obliques, lacking NMDAR-mediated supralinearity, cannot produce large local Ca^{2+} signals without bAPs. This suggests that either the requirements for plasticity vary in these different compartments or that oblique, tuft, and basal dendrites have distinct plasticity capacities. Future experiments should assess the potentiation and depotentiation regimes in different dendrites and the molecular mechanisms that enable different ranges of operations on inputs in these compartments.

Our study provides new evidence that individual pyramidal cells exhibit diverse modes of input-specific decoding, as a result of distinct dendritic integration rules combined with specific input targeting. The anatomical and computational efficiency of this functional architecture, as well as its generality across cortex, represents an exciting future avenue of research.

STAR METHODS

RESOURCE AVAILABILITY

Lead Contact—Correspondence and requests for materials or resources should be addressed to Dr. Mark T. Harnett (harnett@mit.edu).

Materials Availability—This study did not generate any new materials or unique reagents.

Data and Code Availability—The datasets generated during the current study are available from the corresponding author upon request.

The study did not generate any original code.

Any additional information required to reanalyze the data reported in this paper is available from the Lead Contact upon request.

EXPERIMENTAL MODEL AND SUBJECT DETAILS

All animal procedures were carried out in accordance with NIH and Massachusetts Institute of Technology Committee on Animal care guidelines. C57BL/6 male and female mice were used in approximately equal numbers. Adult mice (between 8 and 16 weeks of age) were used for all electrophysiology experiments. 5 12-week old mice were used for rabies tracing experiments. Mice were kept on a 12-hour light/dark cycle in conventional housing and had unrestricted access to food and water.

METHOD DETAILS

Stereotactic Surgery Procedures—Viral injection surgeries were performed using aseptic techniques. Mice were anesthetized with isoflurane and head-secured in a stereotaxic apparatus. Body temperature was maintained with a feedback-controlled heating pad

(DC Temperature Control System, FHC). Slow-release buprenorphine (1 mg/kg) was pre-operatively injected subcutaneously. After incision of the scalp, a small burr hole was made using a dental air drill. Virus was delivered at a slow rate (max. 50 nL/min) to prevent tissue damage through a small beveled injection pipette. After a five-minute rest, the pipette was slowly withdrawn and the incision was sutured. For rabies tracing experiments, a 50 nL 1:1 mixture of pENN-AAV1-CamKII(0.4)-CRE-SV40 (105558-AAV1; Addgene) and AAV1-hsyn-DIO-TVA66T-dTom-CVS-N2C(g) (Allen Institute) was unilaterally delivered to layer 5 A30 RSC (stereotaxtic coordinates in mm on the antero-posterior axis (AP) from Bregma: −2.7; medio-lateral axis (ML): +0.7; and dorso-ventral (DV): +0.45). After 3 weeks of expression, 100 nL of the modified rabies virus (EnvA dG CVS-N2C Histone-eGFP, Allen Institute) was injected at the same site and allowed to express for 9 days before processing for histological analysis. For sCRACM experiments, bilateral injections of 100 nL of AAV2-hSyn-hChR2(H134R)-mCherry (UNC Vector Core) were made over M2 (AP: −0.5; ML: +/− 0.65; DV: 0.50), LD (AP: −1.3; ML: +/− 1.4; DV: 2.45), or V1 (AP −3 and −3.8, ML +/−2.4 and +/− 2.8, DV: 0.45 and 0.5). For V1 injections, two small burr holes were drilled to increase the spread of infection (see Supplementary Fig. S2 for 3D reconstructions of the injection coordinates for all sites from recovered brain slices). Virus was allowed to express for 4–8 weeks before slice electrophysiology experiments commenced. For anterograde fiber tracing from V1 and M2, mice received bilateral stereotaxic injections in V1 and M2 with same coordinates as described above of 100 nL of pENN-AAV-CAG-tdTomato-WPRE-SV40 (105554-AAV1; Addgene). The virus expressed for 10 days before perfusion.

Immunohistochemistry and confocal imaging—For monosynaptic rabies tracing and M2 and V1 fiber density quantification experiments, brains of injected mice were fixed by transcardial perfusion with 4% paraformaldehyde in PBS and left overnight at 4°C. Brains were sectioned coronally at 100 μm thickness with a floating section vibratome (Leica VT1000s). Sections from rabies tracing experiments were rinsed in PBS and then immunolabeled with 1:1000 DAPI solution (62248; Thermo Fisher Scientific). Sections from M2 and V1 fiber density experiments were rinsed in PBS, blocked in 2% normal goat serum and 0.4% Triton x-100 for 1 hour, and immunolabeled with 1:500 rabbit anti-RCFP (632475; Takara) for 24 hours at 4°C. Sections were rinsed 3 times for 10 minutes with 0.4% Triton x-100 in PBS (PBST), incubated in 1:250 Alexa Fluor 568 goat anti-rabbit IgG (H+L) (A-11036; Thermo Fisher Scientific) for 3 hours, and raised in PBST.

For LD fiber density quantification and sCRACM injection site verification, slices recovered from sCRACM experiments preparations were rapidly transferred to well plates containing 4% paraformaldehyde and left overnight at 4°C. They were subsequently rinsed 1 time with PBS for 10 minutes. Sections containing RSC and the injection areas were immunolabeled with 1:1000 DAPI solution for 5 minutes. All sections were mounted and coverslipped with clear-mount with tris buffer (17985–12; Electron Microscopy Sciences). Confocal images were captured using a Leica TCS SP8 microscope with a 10X objective (NA 0.40) and a Zeiss LSM 710 with a 10x objective (NA 0.45).

Confocal Image Processing—The spread and targeting of V1, M2 and LD areas were verified from the recovered sCRACM brain slices containing the injection sites, visible from high density of cells with mCherry expression. The center of mass of the injection volumes was determined by visual inspection, aligned with the confocal images of the injection sites to the Mouse Allen Reference Atlas, and measured with ImageJ software for AP, ML and DV coordinates. Mice with restricted and comparable ChR2-mcherry expression in the target areas were included for quantifications LD fiber density and sCRACM analysis.

Axonal terminals from LD were readily detectable in RSC both under 2-photon and confocal microscopy, but M2 and V1 fibers required antibody enhancement. Therefore, separate anterograde tracing experiments were performed on an additional set of mice. Columnar distributions of axon terminals from infected LD, V1, and M2 cells were obtained from pixel intensity using ImageJ. An area containing a width of 60 pixels and a length of 800 μm, starting at the pia, was drawn across RSC A30. This analysis was divided into anterior (AP=−2.055 to −2.555 mm) and posterior (AP= −2.78 to −3.68 mm) A30. Both hemispheres were sampled for fiber density analysis in each brain section. The average pixel fluorescence was extracted across the area using the plot profile tool.

Successful monosynaptic rabies tracing experiments were determined by restriction of the td-Tomato-labeled starter cells to layer 5 in A30. After alignment to the Allen Mouse Brain Reference Atlas and background removal, presynaptic cells (green) from V1, M2 and LD areas from the same AP coordinates across the 5 mice were counted by segmenting the image using MatLab's watershed function.

Acute slice preparation—Coronal brain slices (300 μm) from retrosplenial cortex were prepared from 8 to 16-week-old C57/BL6 mice of both sexes (Jackson). Animals were deeply anesthetized with isoflurane prior to cardiac perfusion (using slicing solution described below) or decapitation. Slicing was performed with a vibratome (Leica VT1200s) in ice-cold slicing solution containing (in mM): sucrose 90, NaCl 60, $NaHCO_3$ 26.5, KCl 2.75, NaH_2PO_4 1.25, $CaCl_2$ 1.1, $MgCl_2$ 5, glucose 9, sodium pyruvate 3, and ascorbic acid 1, saturated with 95% O_2 and 5% CO_2. Slices were incubated in artificial cerebrospinal fluid (aCSF) containing (in mM): NaCl 120, KCl 3, $NaHCO_3$ 25, NaH_2PO_4 1.25, $CaCl_2$ 1.2, $MgCl_2$ 1.2, glucose 11, sodium pyruvate 3, and ascorbic acid 1, saturated with 95% O_2 and 5% CO_2 at 35.5 °C for 45 min and then stored at 18 °C. All recordings were performed at 33–37 °C in aCSF.

Electrophysiological recordings—An Olympus BX-61 microscope with infrared Dodt optics and a water-immersion lens (60X, 0.9 NA; Olympus) was used to visualize cells. Patch-clamp recordings were performed from morphologically and electrophysiologically identified L5b RSC pyramidal cells. Current-clamp recordings were performed in bridge mode with a Dagan BVC-700 amplifier with bridge fully balanced. Current and voltage signals were filtered at 10 kHz and digitized at 20 kHz. Patch pipettes were prepared with thin-wall glass (1.5 O.D., 1.1 I.D.). Pipettes had resistances ranging from 6 to 12 MΩ and the capacitance was fully neutralized prior to break in. The standard intracellular solution contained (in mM): potassium gluconate 134, KCl 6, HEPES buffer 10, NaCl 4, Mg_2ATP 4, NaGTP 3, and phosphocreatine di (tris) 14. Depending on the experiment, 0.05 Alexa 594,

0.1 Alexa 488, and/or 0.1 OGB 6F mM (Invitrogen) were added to the internal solution. Liquid junction potential was not corrected for.

Subcellular Channelrhodopsin Assisted Circuit Mapping (sCRACM)—Prior to starting each sCRACM experiment, we verified viral targeting with 2-photon imaging by visualizing fluorescently labeled cell bodies at injection locations in acute slices. For all recordings TTX (500 nM), 4-AP (100 μM), and CPP (5 μM) were added to the bath perfusion to limit spatial activation of presynaptic terminals. After whole-cell break in, a full-field 473 nm LED (ThorLabs) was used to determine if the cell received inputs to the region where the injection was performed. If a reliable EPSP could be obtained with the full-field LED, we proceeded to sCRACM. The position of a 473 nm laser beam (OptoEngine LLC, 100mW) was controlled with galvanometer scanners (Bruker). The beam passed through an air objective (4x, 0.16 NA; UPlanApo, Olympus). The duration of the light pulses was controlled via TTL input to the laser. Duration was adjusted to obtain small EPSPs (1–4 mV); the interstimulus interval between each spot was 1 s. Stimulation used a 50 μm spot spacing in a grid of 15 × 20 spot (750 μm × 1000 μm), which covered the dendritic arbor. Grids were repeated 2–6 times and averaged. sCRACM pixel values (EPSP amplitude) were calculated as the difference between local baseline (mean voltage 50ms before stimulation) and maximum voltage in a 50 ms window after photo stimulation. Population data of the spatial distribution of inputs were analyzed by first rotating the maps to align all neurons (to vertical trunk dendrites), then peak-normalizing the maps, and finally averaging across cells within a given experiment (LD vs. V1 vs. M2).

Simultaneous two-photon glutamate uncaging and Ca^{2+} imaging—A two-photon laser scanning system (Bruker) with dual galvanometers and two Mai-Tai lasers were used to simultaneously image and uncage glutamate. One laser path was used to image Alexa 594 at 880 nm or OGB 6F and Alexa 488 at 920 nm (separated via dichroic mirrors to independent GaAsP PMTs). Linescan imaging of spines and dendrites was performed at 700–1300 Hz with dwell times of 8 μs for <400 ms. The second path was used to photolyse 4-methoxy-7-nitroindolinyl-caged-L-glutamate (MNI-glutamate) at 720 nM. Stock MNI solutions (50 mM) were freshly diluted in aCSF to 10 mM and applied via pressure ejection through a large glass pipette above the slice. Laser beam intensity was independently controlled with electro-optical modulators (model 350–50; Conoptics). Uncaging dwell time was 0.2 ms. For experiments involving near-simultaneous activation of multiple spines, the interval between spines was 0.32 ms (0.2 ms dwell time and 0.12 ms moving time). Laser beam intensity was independently controlled with electro-optical modulators (model 350–50; Conoptics).

Particular care was taken to limit photodamage during imaging and uncaging. This included the use of a passive 8× pulse splitter in the uncaging path in all experiments to drastically reduce photodamage(Ji, Magee and Betzig, 2008). Basal fluorescence of both channels was continuously monitored as an immediate indicator of damage to cellular structures. Subtle signs of damage included decreases in or loss of phasic Ca^{2+}signals in response to either uncaging or current injection, small but persistent depolarization following uncaging, and

changes in the kinetics of voltage responses to uncaging or current injection. Experiments were terminated if neurons exhibited any of these phenomena.

Ca^{2+} signals are expressed as $\Delta F/F$ (calculated as $(F - F_{baseline})/F_{baseline}$). Data was collected from dendrites that were at least 30 μm (and up to 150 μm) below the surface of the slice that were not prematurely cut off before termination. Input-output experiments were done with individual spine uEPSP summation, but for distal tuft branches, it was necessary to group 3 to 5 spines together to circumvent electrical filtering and record larger "unitary" uEPSPs without saturating the synapses. Uncaging experiments were aligned together for group analysis using the local branch Ca^{2+} signals; in oblique dendrites, this was always when an AP was produced. In the hyperpolarization experiments in Fig. 6A–C, branches were aligned to the threshold number of inputs for local branch Ca^{2+} signals and APs prior to hyperpolarization.

Measurement of AMPA-to-NMDA receptor ratio at individual spines— Experiments in Fig. 7 were conducted as described for glutamate uncaging above, except no Ca^{2+} indicator was included in the ICS and stock MNI-caged glutamate solution (50 mM) was freshly diluted in Mg^{+2} -free aCSF to 10 mM. Uncaging locations were chosen so that they were located 0.5 μm from the center of individual spine heads in the radial direction. 7–18 spines were individually stimulated at each branch. The uncaging stimulus was delivered in each spine separately (using an isi of 500 ms). Unitary uEPSPs were evoked 10 to 22 times and responses were averaged. Mg^{+2} free aCSF containing 20 μM DNXQ was then washed on for at least 15 minutes. The same uncaging protocol was repeated at the same spines. Care was taken to maintain the initial uncaging locations throughout the experiment.

Focal synaptic stimulation—Theta-glass bipolar stimulating electrodes were filled with Alexa Fluor 488 for visualization and positioned near dendritic branches under two-photon guidance. Stimuli were delivered with an AMPI Isoflex isolator. Intensity was adjusted to generate EPSPs of 0.5–3 mV. For double- and triple-pulse experiments, ISIs of 10 to 20 ms were used and stimulus intensity was increased until an action potential was initiated, as previously reported (Schiller *et al.*, 2000; Larkum, Nevian, Sandler, Polsky, and Schiller, 2009; Polsky, Mel and Schiller, 2009).

Pharmacology—D-APV, MK-801, TTX, 4-AP, and DNQX were dissolved in water. Picrotoxin was dissolved in aCSF and sonicated on the day of the experiment. Persistent blockade of NMDARs was obtained with a combination of 50 μM D-APV (competitive) and 10 μM MK-801 (non-competitive). For acute blockade of NMDARs, 50 μM D-APV was washed on for at least 10 min. For partial blockade of AMPA receptors DNQX was used at 2 μM.

QUANTIFICATION AND STATISTICAL ANALYSIS

Analyses were performed using custom-written MATLAB code. Current and voltage signals were filtered at 2 kHz with zero-phase filtering using the MATLAB function filtfilt. The example voltage traces in Fig. 5 were additionally filtered with a Butterworth filter with a cutoff normalized frequency of 0.1 and the calcium ΔF/F traces with a cutoff of 0.2

to highlight the voltage and calcium dynamics. Linescan signals were smoothed using a 2–4 point moving average. Morphological and distance measurements were performed using ImageJ/FIJI (National Institutes of Health) on two-dimensional maximal intensity projections of Z-series collected at the end of the experiment.

Statistical analysis was performed in GraphPad Prism and/or MatLab. For statistical comparisons and mean reporting for the uncaging experiments in Fig. 3, 4, 5 and 6 the two groups of inputs of maximum gain excluding AP and that contained all branches were used; for Supplementary Fig. S4 gain and ΔF/F values corresponding to 26–31 inputs were used. Unless otherwise stated, results are presented as mean±SE, with the exception of AMPA:NMDA and the presynaptic cell density results, which are presented as median, lower, and upper quartiles (Q1–Q3). Statistical details can be found in the text and/or figure legends. Reported n values refer to number of branches unless indicated otherwise.

Supplementary Material

Refer to Web version on PubMed Central for supplementary material.

Acknowledgements

We thank Hongkui Zeng, Shenqin Yao, Ali Cetin, and the Allen Institute for sharing monosynaptic rabies tracing viral constructs, and Courtney Yaeger, Jaeyoung Yoon, Valerio Francioni, and Michael Roberts for constructive criticism on the manuscript. D.V. is supported by a Boehringer Ingelheim Fonds PhD Fellowship (D.V). M.T.H. is supported by the NIH (RO1NS106031) and the James W. and Patricia T. Poitras Fund at MIT. M.T.H. is a Klingenstein-Simons Fellow, a Vallee Foundation Scholar, and a McKnight Scholar.

References

Abrahamsson T et al. (2012) ‘Thin Dendrites of Cerebellar Interneurons Confer Sublinear Synaptic Integration and a Gradient of Short-Term Plasticity’, Neuron. Elsevier Inc, 73(6), pp. 1159–1172. doi: 10.1016/j.neuron.2012.01.027.

Alexander AS et al. (2020) ‘Egocentric boundary vector tuning of the retrosplenial cortex’, Science Advances, 6(8). doi: 10.1126/sciadv.aaz2322.

Alexander AS and Nitz DA (2015) ‘Retrosplenial cortex maps the conjunction of internal and external spaces’, Nature Neuroscience, 18(8), pp. 1143–1151. doi: 10.1038/nn.4058. [PubMed: 26147532]

Andrásfalvy BK and Magee JC (2001) ‘Distance-dependent increase in AMPA receptor number in the dendrites of adult hippocampal CA1 pyramidal neurons’, Journal of Neuroscience, 21(23), pp. 9151–9159. doi: 10.1523/jneurosci.21-23-09151.2001. [PubMed: 11717348]

Ariav G, Polsky A and Schiller J (2003) ‘Submillisecond precision of the input-output transformation function mediated by fast sodium dendritic spikes in basal dendrites of CA1 pyramidal neurons’, Journal of Neuroscience, 23(21), pp. 7750–7758. doi: 10.1523/jneurosci.23-21-07750.2003. [PubMed: 12944503]

Bathellier B, Margrie TW and Larkum ME (2009) ‘Properties of piriform cortex pyramidal cell dendrites: Implications for olfactory circuit design’, Journal of Neuroscience, 29(40), pp. 12641–12652. doi: 10.1523/JNEUROSCI.1124-09.2009. [PubMed: 19812339]

Beaulieu-Laroche L et al. (2018) ‘Enhanced Dendritic Compartmentalization in Human Cortical Neurons’, Cell. Elsevier, 175(3), pp. 643–651.e14. doi: 10.1016/j.cell.2018.08.045.

Beaulieu-Laroche L and Harnett MT (2018) ‘Dendritic Spines Prevent Synaptic Voltage Clamp’, Neuron. Elsevier Inc, 97(1), pp. 75–82.e3. doi: 10.1016/j.neuron.2017.11.016.

Bittner KC et al. (2015) ‘Conjunctive input processing drives feature selectivity in hippocampal CA1 neurons’, Nature Neuroscience, 18(8), pp. 1133–1142. doi: 10.1038/nn.4062. [PubMed: 26167906]

Bittner KC et al. (2017) ‘Behavioral time scale synaptic plasticity underlies CA1 place fields’, Science, 357(6355), pp. 1033–1036. doi: 10.1126/science.aan3846. [PubMed: 28883072]

Branco Tiago, Clark Beverley A., Häusser M (2010) ‘Dendritic Discrimination of Temporal Input Sequences in Cortical Neurons’, Science, 329(September), pp. 1671–1676. [PubMed: 20705816]

Branco T and Häusser M (2011) ‘Synaptic Integration Gradients in Single Cortical Pyramidal Cell Dendrites’, Neuron, 69(5), pp. 885–892. doi: 10.1016/j.neuron.2011.02.006. [PubMed: 21382549]

Brandalise F et al. (2016) ‘Dendritic NMDA spikes are necessary for timing-dependent associative LTP in CA3 pyramidal cells’, Nature Communications. Nature Publishing Group, 7, pp. 1–9. doi: 10.1038/ncomms13480.

Chen WR, Midtgaard J and Shepherd GM (1997) ‘Forward and backward propagation of dendritic impulses and their synaptic control in mitral cells’, Science, 278(5337), pp. 463–467. doi: 10.1126/science.278.5337.463. [PubMed: 9334305]

Cho J and Sharp PE (2001) ‘Head direction, place, and movement correlates for cells in the rat retrosplenial cortex’, Behavioral Neuroscience, 115(1), pp. 3–25. doi: 10.1037/0735-7044.115.1.3. [PubMed: 11256450]

Dembrow NC, Zemelman BV and Johnston D (2015) ‘Temporal dynamics of l5 dendrites in medial prefrontal cortex regulate integration versus coincidence detection of afferent inputs’, Journal of Neuroscience, 35(11), pp. 4501–4514. doi: 10.1523/JNEUROSCI.4673-14.2015. [PubMed: 25788669]

Fischer LF et al. (2019) ‘Representation of visual landmarks in retrosplenial cortex’, bioRxiv, pp. 1–25. doi: 10.1101/811430.

Gale SD and Murphy GJ (2016) ‘Active dendritic properties and local inhibitory input enable selectivity for object motion in mouse superior colliculus neurons’, Journal of Neuroscience, 36(35), pp. 9111–9123. doi: 10.1523/JNEUROSCI.0645-16.2016. [PubMed: 27581453]

Gambino F et al. (2014) ‘Sensory-evoked LTP driven by dendritic plateau potentials in vivo’, Nature, 515(7525), pp. 116–119. doi: 10.1038/nature13664. [PubMed: 25174710]

Gordon U, Polsky A and Schiller J (2006) ‘Plasticity compartments in basal dendrites of neocortical pyramidal neurons’, Journal of Neuroscience, 26(49), pp. 12717–12726. doi: 10.1523/JNEUROSCI.3502-06.2006. [PubMed: 17151275]

Van Groen T and Wyss JM (2003) ‘Connections of the retrosplenial granular b cortex in the rat’, Journal of Comparative Neurology, 463(3), pp. 249–263. doi: 10.1002/cne.10757.

Hall BJ and Ghosh A (2008) ‘Regulation of AMPA receptor recruitment at developing synapses’, Trends in Neurosciences, 31(2), pp. 82–89. doi: 10.1016/j.tins.2007.11.010. [PubMed: 18201773]

Harnett MT et al. (2012) ‘Synaptic amplification by dendritic spines enhances input cooperativity’, Nature. Nature Publishing Group, 491(600), pp. 3–9. doi: 10.1038/nature11554.

Harnett MT et al. (2013) ‘Potassium channels control the interaction between active dendritic integration compartments in layer 5 cortical pyramidal neurons’, Neuron. Elsevier Inc., 79(3), pp. 516–529. doi: 10.1016/j.neuron.2013.06.005. [PubMed: 23931999]

Harnett MT, Magee JC and Williams SR (2015) ‘Distribution and function of HCN channels in the apical dendritic tuft of neocortical pyramidal neurons’, Journal of Neuroscience, 35(3), pp. 1024–1037. doi: 10.1523/JNEUROSCI.2813-14.2015. [PubMed: 25609619]

Harvey CD, Coen P and Tank DW (2012) ‘Choice-specific sequences in parietal cortex during a virtual-navigation decision task’, Nature. Nature Publishing Group, 484(7392), pp. 62–68. doi: 10.1038/nature10918. [PubMed: 22419153]

Harvey CD and Svoboda K (2007) ‘Locally dynamic synaptic learning rules in pyramidal neuron dendrites’, Nature, 450(7173), pp. 1195–1200. doi: 10.1038/nature06416. [PubMed: 18097401]

Histed MH, Bonin V and Reid RC (2009) ‘Direct Activation of Sparse, Distributed Populations of Cortical Neurons by Electrical Microstimulation’, Neuron. Elsevier Ltd, 63(4), pp. 508–522. doi: 10.1016/j.neuron.2009.07.016. [PubMed: 19709632]

Iacaruso MF, Gasler IT and Hofer SB (2017) ‘Synaptic organization of visual space in primary visual cortex’, Nature. Nature Publishing Group, 547(7664), pp. 449–452. doi: 10.1038/nature23019. [PubMed: 28700575]

Jacob P-Y et al. (2017) 'An independent, landmark-dominated head-direction signal in dysgranular retrosplenial cortex.', Nature neuroscience. Nature Publishing Group, 20(2), pp. 173–175. doi: 10.1038/nn.4465. [PubMed: 27991898]

Ji N, Magee JC and Betzig E (2008) 'High-speed, low-photodamage nonlinear imaging using passive pulse splitters', Nature Methods, 5(2), pp. 197–202. doi: 10.1038/nmeth.1175. [PubMed: 18204458]

Ju N et al. (2020) 'Spatiotemporal functional organization of excitatory synaptic inputs onto macaque V1 neurons', Nature Communications. Springer US, 11(1). doi: 10.1038/s41467-020-14501-y.

Kalmbach BE et al. (2013) 'Dendritic generation of mGluR-mediated slow afterdepolarization in layer 5 neurons of prefrontal cortex', Journal of Neuroscience, 33(33), pp. 13518–13532. doi: 10.1523/JNEUROSCI.2018-13.2013. [PubMed: 23946410]

Katona G et al. (2011) 'Roller coaster scanning reveals spontaneous triggering of dendritic spikes in CA1 interneurons', Proceedings of the National Academy of Sciences of the United States of America, 108(5), pp. 2148–2153. doi: 10.1073/pnas.1009270108. [PubMed: 21224413]

Kauer JA, Malenka RC and Nicoll RA (1988) 'A persistent postsynaptic modification mediates long-term potentiation in the hippocampus', Neuron, 1(10), pp. 911–917. doi: 10.1016/0896-6273(88)90148-1. [PubMed: 2908443]

Kim EJ et al. (2015) 'Three Types of Cortical Layer 5 Neurons That Differ in Brain-wide Connectivity and Function Article Three Types of Cortical Layer 5 Neurons That Differ in Brain-wide Connectivity and Function', Neuron. Elsevier Inc., 88(6), pp. 1253–1267. doi: 10.1016/j.neuron.2015.11.002. [PubMed: 26671462]

Knight R and Hayman R (2014) 'Allocentric directional processing in the rodent and human retrosplenial cortex', Frontiers in Human Neuroscience, 8(MAR), pp. 1–5. doi: 10.3389/fnhum.2014.00135. [PubMed: 24474914]

Krueppel R, Remy S and Beck H (2011) 'Dendritic integration in hippocampal dentate granule cells', Neuron. Elsevier Inc., 71(3), pp. 512–528. doi: 10.1016/j.neuron.2011.05.043. [PubMed: 21835347]

Kumar A et al. (2018) 'Nmda spikes mediate amplification of odor pathway information in the piriform cortex', eLife, pp. 1–24. doi: 10.1101/346791.

Kumar SS and Huguenard JR (2003) 'Pathway-Specific Differences in Subunit Composition of Synaptic NMDA Receptors on Pyramidal Neurons in Neocortex', Journal of Neuroscience, 23(31), pp. 10074–10083. doi: 10.1523/jneurosci.23-31-10074.2003. [PubMed: 14602822]

Labarrera C et al. (2018) 'Adrenergic Modulation Regulates the Dendritic Excitability of Layer 5 Pyramidal Neurons In Vivo', Cell Reports. ElsevierCompany, 23(4), pp. 1034–1044. doi: 10.1016/j.celrep.2018.03.103.

Larkum M (2013) 'A cellular mechanism for cortical associations: An organizing principle for the cerebral cortex', Trends in Neurosciences. Elsevier Ltd, 36(3), pp. 141–151. doi: 10.1016/j.tins.2012.11.006. [PubMed: 23273272]

Larkum ME et al. (2009) 'Synaptic Integration in Tuft Dendrites of Layer 5 Pyramidal Neurons:A New Unifying Principle', Science, 756(2009), pp. 756–761.

Larkum ME, Zhu JJ and Sakmann B (1999) 'A new cellular mechanism for coupling inputs arriving at different cortical layers', Nature, 398(6725), pp. 338–341. doi: 10.1038/18686. [PubMed: 10192334]

Lavzin M et al. (2012) 'Nonlinear dendritic processing determines angular tuning of barrel cortex neurons in vivo', Nature. Nature Publishing Group, 490(7420), pp. 397–401. doi: 10.1038/nature11451. [PubMed: 22940864]

London M and Häusser M (2005) 'Dendritic computation', Annual Review of Neuroscience, 28, pp. 503–532. doi: 10.1146/annurev.neuro.28.061604.135703.

Losonczy A and Magee JC (2006) 'Integrative Properties of Radial Oblique Dendrites in Hippocampal CA1 Pyramidal Neurons', Neuron, 50(2), pp. 291–307. doi: 10.1016/j.neuron.2006.03.016. [PubMed: 16630839]

Losonczy A, Makara JK and Magee JC (2008) 'Compartmentalized dendritic plasticity and input feature storage in neurons', Nature, 452(March). doi: 10.1038/nature06725.

Major G et al. (2008) ‘Spatiotemporally graded NMDA spike/plateau potentials in basal dendrites of neocortical pyramidal neurons’, Journal of Neurophysiology, 99(5), pp. 2584–2601. doi: 10.1152/jn.00011.2008. [PubMed: 18337370]

Major G, Larkum ME and Schiller J (2013) ‘Active properties of neocortical pyramidal neuron dendrites’, Annual Review of Neuroscience, 36, pp. 1–24. doi: 10.1146/annurev-neuro-062111-150343.

Malinow R and Malenka RC (2002) ‘AMPA receptor trafficking and synaptic plasticity’, Annual Review of Neuroscience, 25, pp. 103–126. doi: 10.1146/annurev.neuro.25.112701.142758.

Mante V et al. (2013) ‘Context-dependent computation by recurrent dynamics in prefrontal cortex’, Nature. Nature Publishing Group, 503(7474), pp. 78–84. doi: 10.1038/nature12742. [PubMed: 24201281]

Markram H, Helm PJ and Sakmann B (1995) ‘Dendritic calcium transients evoked by single back-propagating action potentials in rat neocortical pyramidal neurons.’, The Journal of Physiology, 485(1), pp. 1–20. doi: 10.1113/jphysiol.1995.sp020708. [PubMed: 7658365]

Mel BW (1991) ‘The clusteron: Toward a simple abstraction for a complex neuron’, Nips, pp. 35–42.

Migliore M and Shepherd GM (2002) ‘Emerging rules for the distributions of active dendritic conductances’, Nature Reviews Neuroscience, 3(5), pp. 362–370. doi: 10.1038/nrn810. [PubMed: 11988775]

Miller AMP et al. (2014) ‘Cues, context, and long-term memory: the role of the retrosplenial cortex in spatial cognition’, Frontiers in Human Neuroscience, 8(August), pp. 1–15. doi: 10.3389/fnhum.2014.00586. [PubMed: 24474914]

Mitchell AS et al. (2018) ‘Retrosplenial cortex and its role in spatial cognition’, Brain and Neuroscience Advances, 2, p. 239821281875709. doi: 10.1177/2398212818757098.

Nevian T et al. (2007) ‘Properties of basal dendrites of layer 5 pyramidal neurons: A direct patch-clamp recording study’, Nature Neuroscience, 10(2), pp. 206–214. doi: 10.1038/nn1826. [PubMed: 17206140]

Nicholson DA et al. (2006) ‘Distance-Dependent Differences in Synapse Number and AMPA Receptor Expression in Hippocampal CA1 Pyramidal Neurons’, Neuron, 50(3), pp. 431–442. doi: 10.1016/j.neuron.2006.03.022. [PubMed: 16675397]

Van Den Oever MC et al. (2008) ‘Prefrontal cortex AMPA receptor plasticity is crucial for cue-induced relapse to heroin-seeking’, Nature Neuroscience, 11(9), pp. 1053–1058. doi: 10.1038/nn.2165. [PubMed: 19160503]

Palmer LM et al. (2014) ‘NMDA spikes enhance action potential generation during sensory input’, Nature Neuroscience. Nature Publishing Group, 17(3), pp. 383–390. doi: 10.1038/nn.3646. [PubMed: 24487231]

Petreanu L et al. (2009) ‘The subcellular organization of neocortical excitatory connections, Supplementary Information.’, Nature, 457(7233), pp. 1142–5. doi: 10.1038/nature07709. [PubMed: 19151697]

Plotkin JL, Day M and Surmeier DJ (2011) ‘Synaptically driven state transitions in distal dendrites of striatal spiny neurons’, Nature Neuroscience. Nature Publishing Group, 14(7), pp. 881–888. doi: 10.1038/nn.2848. [PubMed: 21666674]

Poirazi P, Brannon T and Mel BW (2003) ‘Pyramidal neuron as two-layer neural network’, Neuron, 37(6), pp. 989–999. doi: 10.1016/S0896-6273(03)00149-1. [PubMed: 12670427]

Poirazi P and Mel BW (2000) ‘Memory capacity of linear vs. nonlinear models of dendritic integration’, Advances in Neural Information Processing Systems, pp. 157–163.

Polsky A, Mel B and Schiller J (2009) ‘Encoding and decoding bursts by NMDA spikes in basal dendrites of layer 5 pyramidal neurons’, Journal of Neuroscience, 29(38), pp. 11891–11903. doi: 10.1523/JNEUROSCI.5250-08.2009. [PubMed: 19776275]

Polsky A, Mel BW and Schiller J (2004) ‘Computational subunits in thin dendrites of pyramidal cells’, Nature Neuroscience, 7(6), pp. 621–627. doi: 10.1038/nn1253. [PubMed: 15156147]

Rall W and Segev I (1985) ‘Space-Clamp Problems When Voltage Clamping Branched Neurons With Intracellular Microelectrodes’, Voltage and Patch Clamping with Microelectrodes, (14), pp. 191–215. doi: 10.1007/978-1-4614-7601-6_9.

Ranganathan GN et al. (2018) 'Active dendritic integration and mixed neocortical network representations during an adaptive sensing behavior', Nature Neuroscience. Springer US, 21(11), pp. 1583–1590. doi: 10.1038/s41593-018-0254-6. [PubMed: 30349100]

Rees CL, Moradi K and Ascoli GA (2017) 'Weighing the Evidence in Peters' Rule: Does Neuronal Morphology Predict Connectivity?', Trends in Neurosciences. Elsevier Ltd, 40(2), pp. 63–71. doi: 10.1016/j.tins.2016.11.007. [PubMed: 28041634]

Rigotti M et al. (2013) 'The importance of mixed selectivity in complex cognitive tasks', Nature. Nature Publishing Group, 497(7451), pp. 585–590. doi: 10.1038/nature12160. [PubMed: 23685452]

Saal D et al. (2003) 'Drugs of abuse and stress trigger a common synaptic adaptation in dopamine neurons', Neuron, 37(4), pp. 577–582. doi: 10.1016/S0896-6273(03)00021-7. [PubMed: 12597856]

Sarafyazd M and Jazayeri M (2019) 'Hierarchical reasoning by neural circuits in the frontal cortex', Science, 364(6441). doi: 10.1126/science.aav8911.

Schiller J et al. (2000) 'NMDA spikes in basal dendrites', Nature, 1261(1997), pp. 285–289.

Schiller J and Schiller Y (2001) 'NMDA receptor-mediated dendritic spikes and coincident signal amplification', Current Opinion in Neurobiology, 11(3), pp. 343–348. doi: 10.1016/S0959-4388(00)00217-8. [PubMed: 11399433]

Scholl B, Wilson DE and Fitzpatrick D (2017) 'Local Order within Global Disorder: Synaptic Architecture of Visual Space', Neuron. Elsevier Inc., 96(5), pp. 1127–1138.e4. doi: 10.1016/j.neuron.2017.10.017. [PubMed: 29103806]

Shibata H (1993) 'Efferent projections from the anterior thalamic nuclei to the cingulate cortex in the rat', Journal of Comparative Neurology, 330(4), pp. 533–542. doi: 10.1002/cne.903300409.

Sivyer B and Williams SR (2013) 'Direction selectivity is computed by active dendritic integration in retinal ganglion cells', Nature Neuroscience. Nature Publishing Group, 16(12), pp. 1848–1856. doi: 10.1038/nn.3565. [PubMed: 24162650]

Spruston Nelson, Jaffe David B, Williams Stephen H. and Johnston D. (1993) 'Voltage- and Space-Clamp Errors Associated With the Measurement of Electrotonically Remote Synaptic Events', Journal of Neurophys, 70(2).

Stuart Greg, Häusser M. (2001) 'Dendritic coincidence detection of EPSPs and action potentials', Nat. Neurosci, 4, pp. 63–71. [PubMed: 11135646]

Stuart G and Spruston N (1998) 'Determinants of voltage attenuation in neocortical pyramidal neuron dendrites', Journal of Neuroscience, 18(10), pp. 3501–3510. doi: 10.1523/jneurosci.18-10-03501.1998. [PubMed: 9570781]

Sugar J et al. (2011) 'The Retrosplenial Cortex: Intrinsic Connectivity and Connections with the (Para)Hippocampal Region in the Rat. An Interactive Connectome', Frontiers in Neuroinformatics, 5(July), pp. 1–13. doi: 10.3389/fninf.2011.00007. [PubMed: 21472085]

Sun Q et al. (2014) 'Dendritic Na+ spikes enable cortical input to drive action potential output from hippocampal CA2 pyramidal neurons', eLife, 3(November), pp. 1–24. doi: 10.7554/eLife.04551.

Tran-Van-Minh A et al. (2015) 'Contribution of sublinear and supralinear dendritic integration to neuronal computations', Frontiers in Cellular Neuroscience, 9(March), pp. 1–15. doi: 10.3389/fncel.2015.00067. [PubMed: 25667569]

Tran-Van-Minh A et al. (2016) 'Differential Dendritic Integration of Synaptic Potentials and Calcium in Cerebellar Interneurons', Neuron, 91(4), pp. 837–850. doi: 10.1016/j.neuron.2016.07.029. [PubMed: 27537486]

Trimmer JS (2015) 'Subcellular localization of K+ channels in mammalian brain neurons: Remarkable precision in the midst of extraordinary complexity', Neuron. Elsevier Inc., 85(2), pp. 238–256. doi: 10.1016/j.neuron.2014.12.042. [PubMed: 25611506]

Ungless MA et al. (2001) 'Single cocaine exposure in vivo induces long-term potentiation in dopamine neurons', Nature, 411(6837), pp. 583–587. doi: 10.1038/35079077. [PubMed: 11385572]

Vann SD, Aggleton JP and Maguire EA (2009) 'What does the retrosplenial cortex do?', Nature Reviews Neuroscience. Nature Publishing Group, 10(11), pp. 792–802. doi: 10.1038/nrn2733. [PubMed: 19812579]

Voigts J and Harnett MT (2020) 'Somatic and Dendritic Encoding of Spatial Variables in Retrosplenial Cortex Differs during 2D Navigation', Neuron. Elsevier Inc., 105(2), pp. 237–245.e4. doi: 10.1016/j.neuron.2019.10.016. [PubMed: 31759808]

Watt AJ et al. (2004) 'A proportional but slower NMDA potentiation follows AMPA potentiation in LTP', Nature Neuroscience, 7(5), pp. 518–524. doi: 10.1038/nn1220. [PubMed: 15048122]

Wickersham IR and Sullivan HA (2015) 'Rabies Viral Vectors for Monosynaptic Tracing and Targeted Transgene Expression in Neurons', Cold Spring Harbor Protocols, pp. 375–386. doi: 10.1101/pdb.prot072389. [PubMed: 25834254]

Williams SR (2004) 'Spatial compartmentalization and functional impact of conductance in pyramidal neurons', Nature Neuroscience, 7(9), pp. 961–967. doi: 10.1038/nn1305. [PubMed: 15322550]

Williams SR and Mitchell SJ (2008) 'Direct measurement of somatic voltage clamp errors in central neurons', Nature Neuroscience, 11(7), pp. 790–798. doi: 10.1038/nn.2137. [PubMed: 18552844]

Williams SR and Stuart GJ (2002) 'Dependence of EPSP efficacy on synapse location in neocortical pyramidal neurons', Science, 295(5561), pp. 1907–1910. doi: 10.1126/science.1067903. [PubMed: 11884759]

Wyss JM and Vangroen T (1992) 'Connections between the retrosplenial cortex and the hippocampal-formation in the rat - a review', Hippocampus, 2(1), pp. 1–12. doi: 10.1002/hipo.450020102. [PubMed: 1308170]

Xu NL et al. (2012) 'Nonlinear dendritic integration of sensory and motor input during an active sensing task', Nature. Nature Publishing Group, 492(7428), pp. 247–251. doi: 10.1038/nature11601. [PubMed: 23143335]

Yamawaki N et al. (2019) 'Long-range inhibitory intersection of a retrosplenial thalamocortical circuit by apical tuft-targeting CA1 neurons', Nature Neuroscience. Springer US, 22(April). doi: 10.1038/s41593-019-0355-x.

Zhang S et al. (2016) 'Organization of long-range inputs and outputs of frontal cortex for top-down control', Nature Neuroscience, 19(12), pp. 1733–1742. doi: 10.1038/nn.4417. [PubMed: 27749828]

Zito K et al. (2009) 'Rapid Functional Maturation of Nascent Dendritic Spines', Neuron. Elsevier Inc., 61(2), pp. 247–258. doi: 10.1016/j.neuron.2008.10.054. [PubMed: 19186167]

Highlights

- Distinct long-range inputs target different dendritic domains of RSC L5 neurons
- Unlike basal and tuft dendrites, apical obliques do not exhibit NMDAR supralinearity
- Increased synaptic AMPA:NMDA underlies linear integration in oblique dendrites

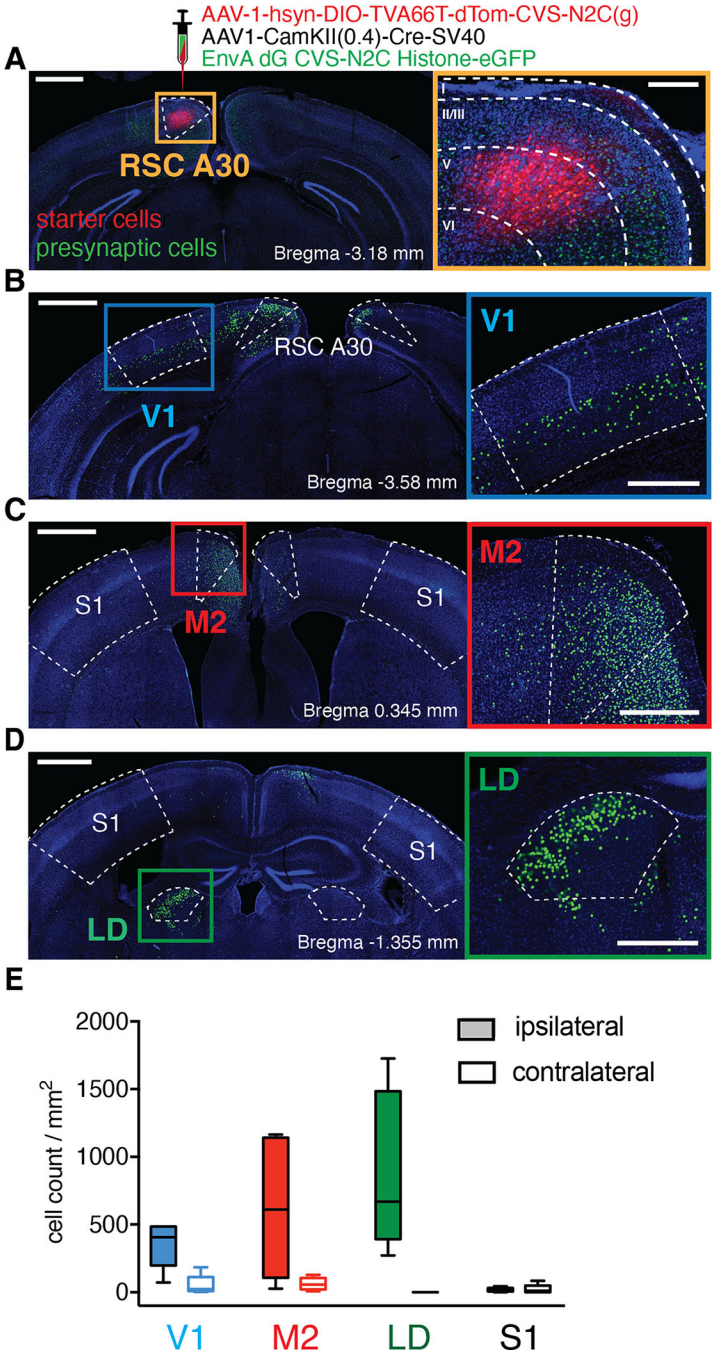

Figure 1: RSC Layer 5 cells receive monosynaptic input from V1, M2, and LD.

A, Unilateral injection of monosynaptic rabies-based retrograde tracing viruses in RSC A30. Left, confocal image of a coronal brain slice at the injection site, starter cells are labeled with tdTomato (red) and presynaptic cells with eGFP (green). Scale bar 0.5 mm. Right: Magnified orange square from left overlaid with cortical layer boundaries (from Allen Brain Atlas) showing starter cell infection localized to layer 5. Scale bar 200 μm. **B**, **C**, **D**, Presynaptic cells were found in V1, M2, and LD, respectively. Left images scale bar 1.0 mm. Right insets: magnified area of interest from right, scale bar 0.5 mm. **E**, Quantification

of presynaptic cells (normalized by area) for V1, M2, LD, and S1 for both ipsi- (filled bars) and contra-lateral (empty bars) hemispheres (n=5 mice). Whisker plots include the medians (center lines), the first interquartile range (boxes) and the ±1.5 × interquartile range (whiskers). Values out of the 99.3 % coverage (outliers) have been excluded.

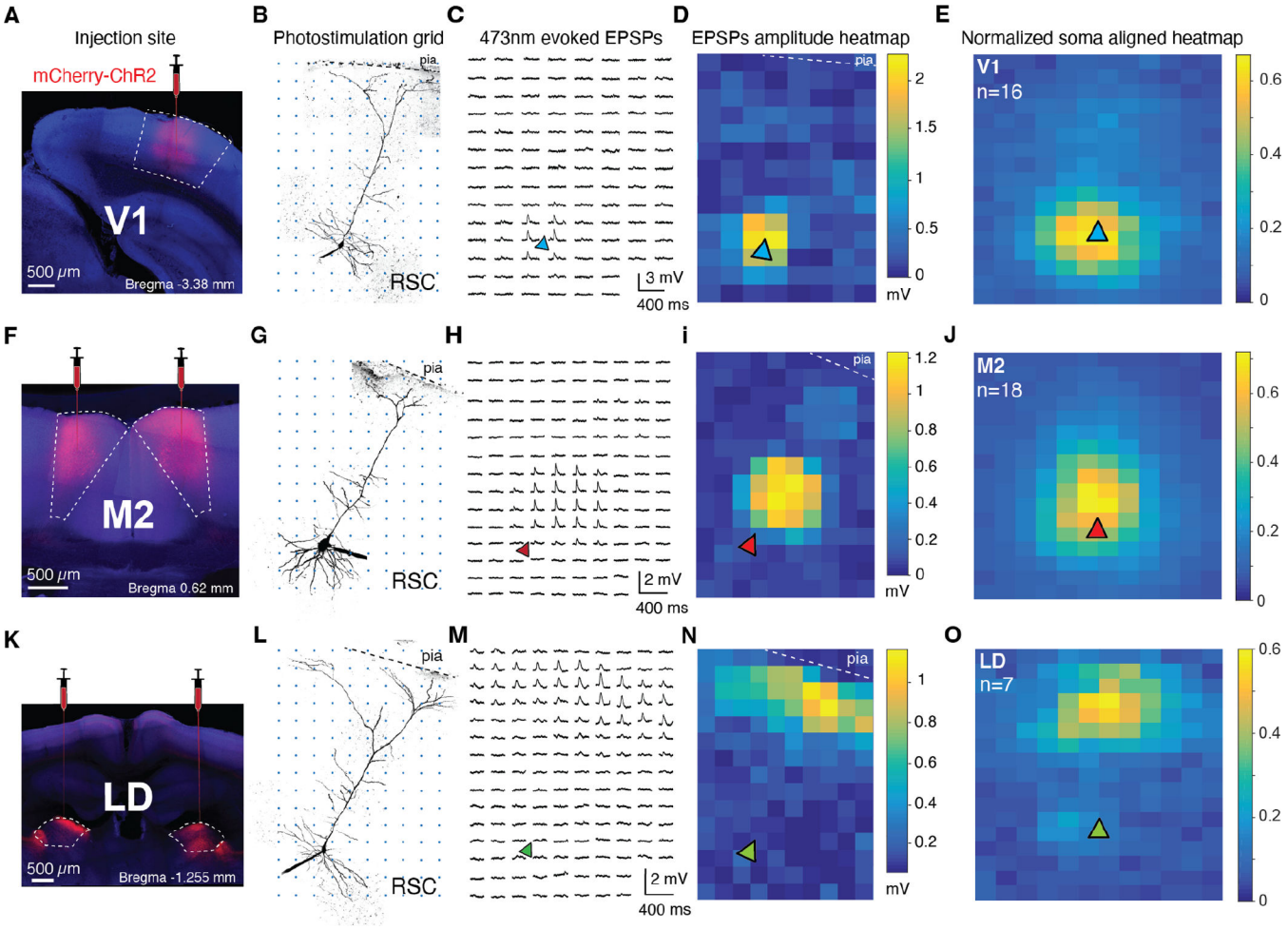

Figure 2: Excitatory monosynaptic inputs from V1, M2, and LD target distinct dendritic domains of RSC A30 L5b PCs.

A, F, K, Coronal slices showing injection sites of AAV2.hSyn-mCherry-ChR2 in V1, M2, and LD, respectively. See Fig. S2 for a summary of injection sites per region. **B, G, L**, Two-photon z-stacks of exemplar RSC A30 L5b PCs from animals injected in V1 (top), M2 (middle), and LD (bottom). Axons from injected brain regions were excited by a 473 nm photo-stimulation grid (50 μm spacing) over the recorded neurons, which were filled with Alexa-488 for post-hoc two-photon reconstruction. **C, H, M**, ChR2-evoked EPSPs from the exemplar cells at left recorded at each photo-stimulation location. EPSPs are only apparent when photo-stimulation spots activate functional synaptic contacts between injected brain regions and recorded cells in RSC. **D, I, N**, Corresponding exemplar heatmaps of EPSP amplitudes for the cells at left. **E, J, O,** Average normalized EPSP amplitude heatmaps aligned to soma position (triangle) for V1 (16 cells from 11 mice), M2 (18 cells from 13 mice), and LD (7 cells from 5 mice).

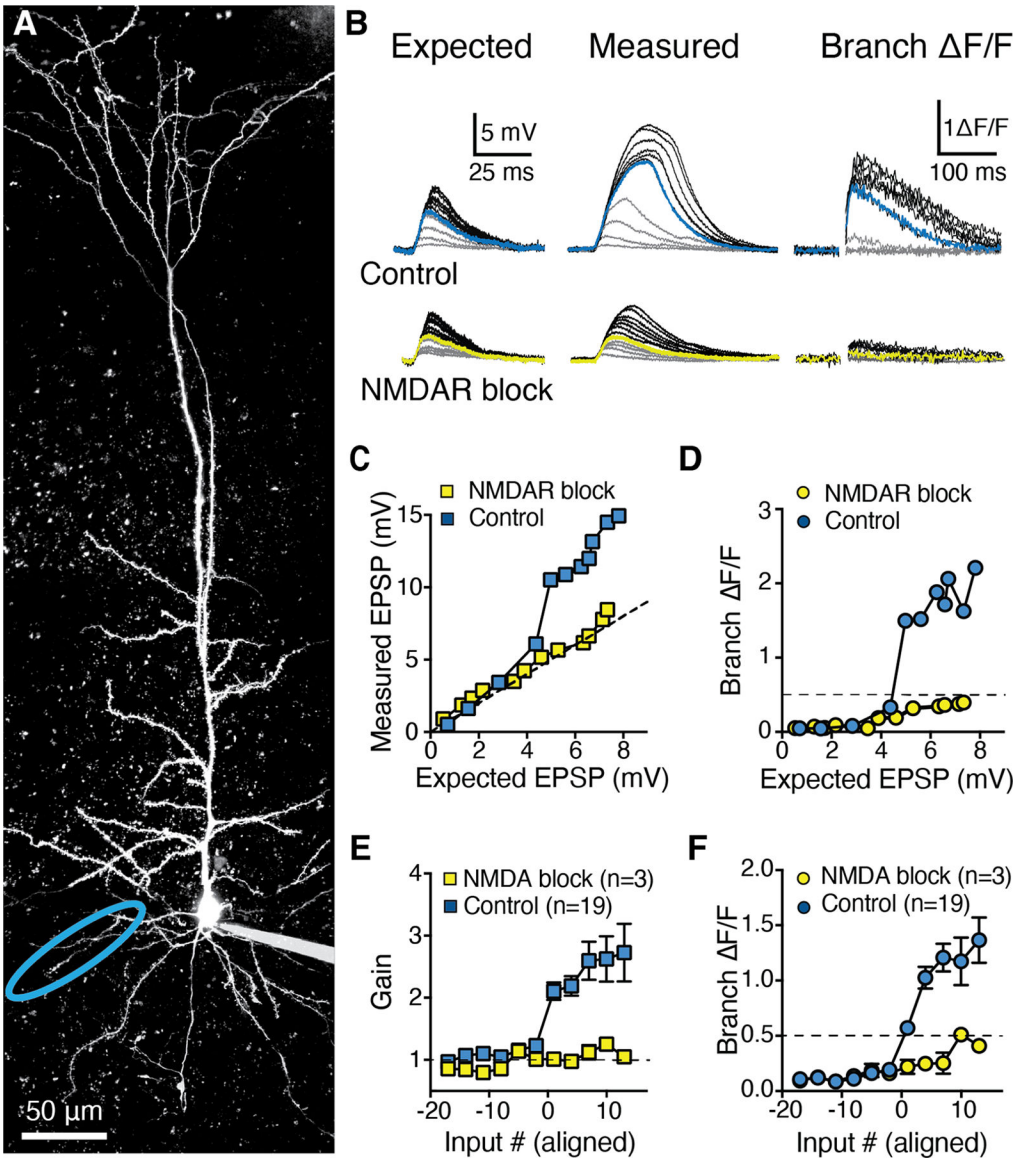

Figure 3: Highly supralinear integration in basal dendrites of RSC A30 L5b PCs mediated by NMDARs.

A, Two-photon z-stack of a L5b RSC A30 PC filled via somatic patch pipette with Alexa-594. **B**, Top: Expected uEPSPs calculated as the linear sum of somatic responses to glutamate uncaging at individual spines (left) versus measured uEPSPs recorded at the soma (middle) and local branch OGB-6F Ca^{2+} signals (right) for synchronous uncaging at increasing numbers of inputs. Blue traces indicate supralinear threshold (>50% ΔF/F) number of inputs in control conditions. Bottom: same as top, but in the presence of D-APV (50 µM) and MK-801 (10 µM) for the same branch. Yellow traces indicate the previous supralinear threshold from top. **C**, Measured uEPSP amplitude and **D**, Local branch ΔF/F, *both* as a function of expected uEPSP amplitude in control condition (blue) and in presence of NMDAR blockers (yellow) for the branch and traces shown in A and B. Dashed line indicates linearity (C) and supralinearity threshold (50% ΔF/F; D). **E**, Population input-output gain in control condition (blue squares, 19 basal branches from 14 neurons) and in

presence of NMDAR blockers (yellow squares, paired experiments in 3 basal branches from 3 neurons), aligned by threshold number of inputs (>50% ΔF/F local branch Ca^{2+}). See also Figure S4. **F**, Corresponding population branch Ca^{2+} signal in control condition and in presence of NMDAR blockers. Data points in E and F are mean±sem.

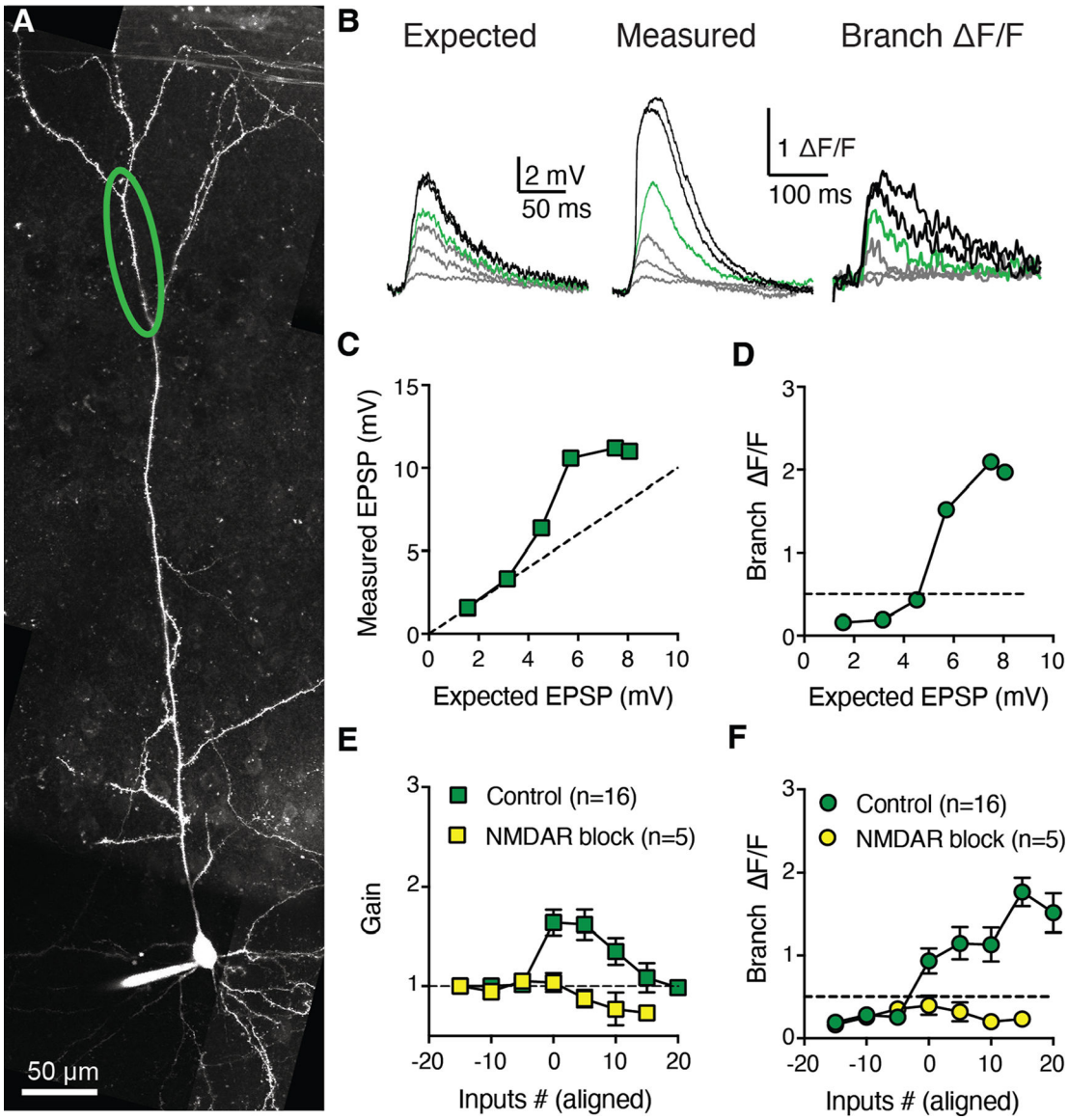

Figure 4: Modest, saturating NMDAR-dependent supralinear integration in tuft dendrites of RSC A30 L5b PCs.

A, Two-photon z-stack of a layer 5b RSC pyramidal neuron filled via somatic patch pipette with Alexa-594. **B**, Expected uEPSPs calculated as the linear sum of somatic responses to glutamate uncaging at individual spines (left). Measured uEPSPs recorded at the soma (middle) and local branch OGB-6F Ca^{2+} signals (right) for synchronous uncaging at increasing numbers of inputs. Green traces indicate supralinear threshold (>50% ΔF/F). **C**, Measured uEPSP amplitude as a function of expected uEPSP amplitude in control condition. Dashed line indicates linearity. **D**, Local branch *ΔF/F as* a function of expected uEPSP amplitude. Dashed line indicates supralinearity threshold (50% ΔF/F). **E**, Population input-output gain in control condition (green squares, 16 tuft branches from 12 L5b RSC neurons) and in presence of NMDAR blockers (yellow squares, paired experiments from 5 tuft branches), aligned by threshold number of inputs. **F**, Corresponding population branch

Ca^{2+} signal relationship in control condition and in presence of NMDAR blockers. Data points in E and F are mean±sem.

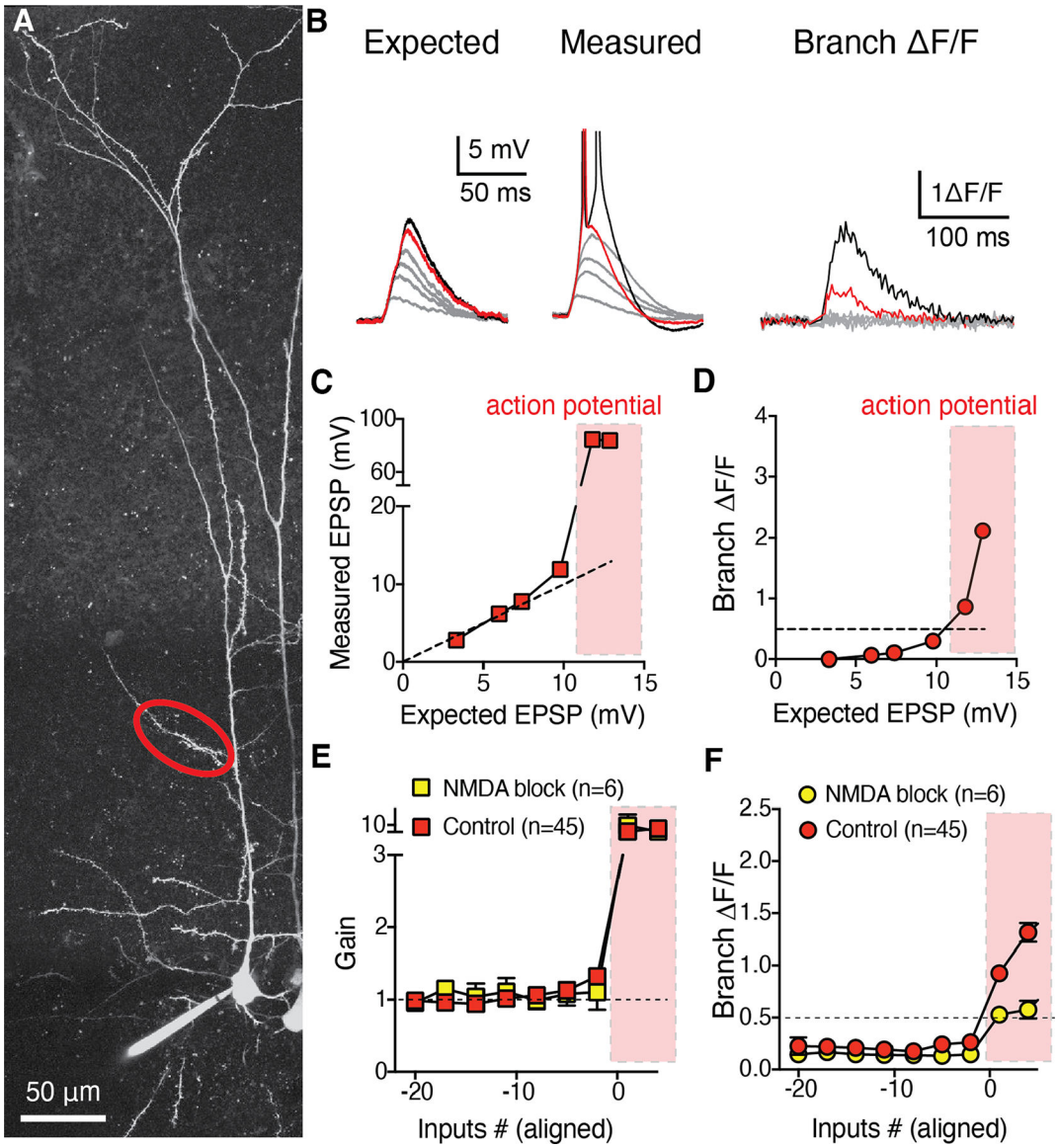

Figure 5: Linear integration in RSC A30 L5b PC oblique dendrites.

A, Two-photon z-stack of an RSC A30 L5b PC filled via somatic patch pipette with Alexa-594 with an oblique branch of interest indicated in red. **B**, Expected uEPSPs calculated as the linear sum of somatic responses to glutamate uncaging at individual spines (left). Measured uEPSPs recorded at the soma (middle) and local branch OGB-6F Ca^{2+} signals (right) for synchronous uncaging at increasing numbers of inputs. Red traces indicate supralinear threshold (>50% ΔF/F) in control conditions concomitant with axonal action potential initiation. **C**, Measured uEPSP amplitude as a function of expected uEPSP amplitude in control condition for the cell, branch, and traces shown in a and b. Dashed line indicates linearity, light red boxes indicate AP initiation. **D**, Local branch *ΔF/F as* a function of expected uEPSP amplitude. Dashed line indicates supralinearity threshold (50% ΔF/F) **E**, Population input-output gain for control (red squares, 45 oblique branches from 34 neurons) and paired NMDAR blockade (yellow squares, 6 branches from 6 neurons),

aligned by threshold. **F**, Corresponding population analysis of branch Ca^{2+} signals. Data points in E and F are mean±sem.

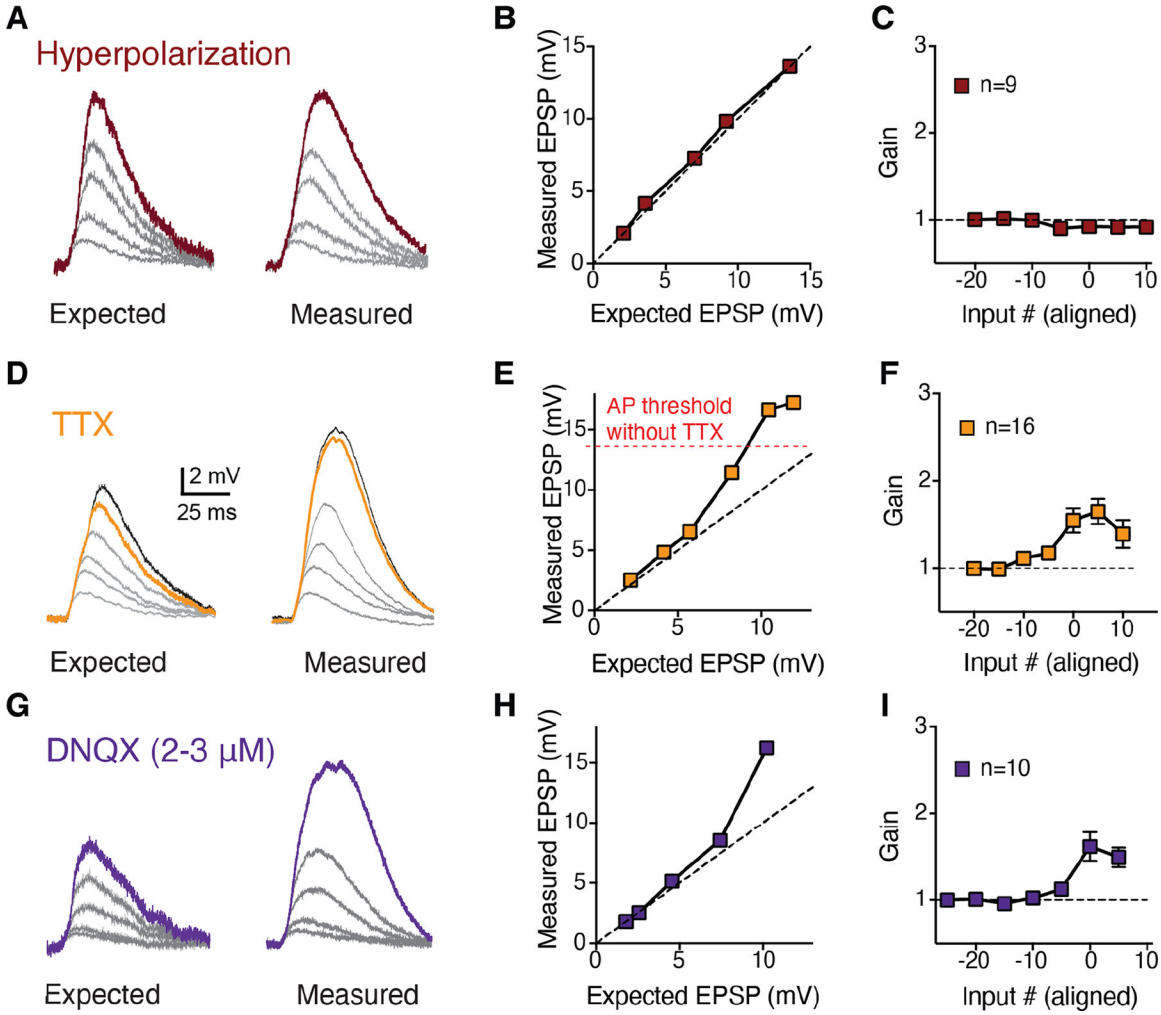

Figure 6: Linear integration in oblique dendrites is consistent with increased synaptic AMPA:NMDA.

A, Example traces of increasing numbers of activated spines for expected (left) and measured (right) uEPSPs after hyperpolarizing the somatic membrane potential to decouple potential branch Na^+ spikes from the axon. **B**, Measured versus expected plot of the data in a. Dashed unity line represents linear integration. **C**, Summary of uEPSP gain as a function of input number for 9 hyperpolarization experiments, aligned by pre-hyperpolarization AP threshold. **D**, Example traces of increasing numbers of activated spines for expected (left) and measured (right) uEPSPs in the presence of TTX to block axonal AP initiation, revealing supralinearity at depolarized potentials previously masked by APs. **E**, Measured versus expected plot of the data in D. **F**, Population input-output gain in TTX for 16 branches, aligned by threshold local branch Ca^{2+} signal. **G**, Example traces of to increasing numbers of activated spines for expected (left) and measured (right) uEPSPs in the presence of subsaturating DNQX to decrease AMPA:NMDA. **H**, Measured versus expected plot of the data in G. **I**, Population input-output gain for 10 subsaturating DNQX experiments shows supralinear branch integration prior to AP initiation. Data points in C, F and I are mean±sem.

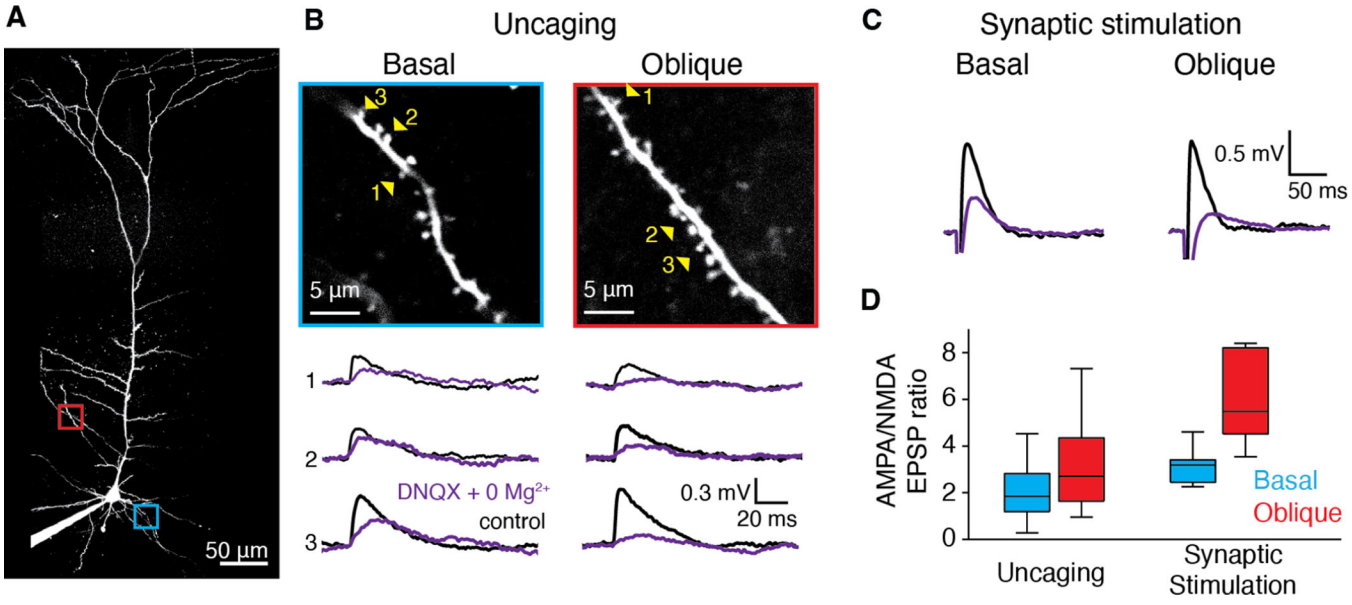

Figure 7: Synapses at apical oblique dendrites exhibit higher AMPA:NMDA receptor ratio than those at basal dendrites.

A, Two-photon z-stack of an RSC A30 L5b PC filled via somatic patch pipette with Alexa-488. Basal branch of interest indicated in blue and oblique branch of interest indicated in red. **B**, Magnified view of basal and oblique branches from A. **C**, Example averaged voltage traces recorded in current clamp mode at the soma in response to glutamate uncaging at individual spines indicated by numbered yellow arrowheads in B, for basal (left) and oblique (right) branches in control aCSF (black) and after wash in of Mg^{+2}-free plus 20 µM DNQX aCSF (purple). **C**, Same as b, but for focal extracellular synaptic stimulation. **D**, Ratio of averaged peak somatic uEPSPs in control and Mg^{+2}-free plus 20 µM DNQX aCSF for uncaging at single spines (left) and focal synaptic stimulation (right). Left: n=66 spines on basal (blue) branches (from 6 cells, 3 mice) versus 64 spines on oblique (red) branches (from 6 cells, 3 mice), p=0.0005, Mann-Whitney U test. Right: n=6 basal (blue) branches (from 6 cells, 4 mice) and 6 oblique (red) branches (from 6 cells, 4 mice) p<0.01, Mann-Whitney U test. Whisker plots show medians (center lines), first interquartile range (boxes) and ±1.5 × interquartile range (whiskers). Values out of the 99.3% coverage (outliers) have been excluded.

KEY RESOURCE TABLE

REAGENT or RESOURCE	SOURCE	IDENTIFIER
Antibodies		
rabbit anti-RCFP	Takara	632475
Alexa Fluor 568 goat anti-rabbit IgG (H+L)	Thermo Fisher Scientific	A-11036
Bacterial and virus strains		
AAV2-hSyn-hChR2(H134R)-mCherry	Karl Deisseroth Lab	UNC Vector Core N/A
pENN-AAV-CAG-tdTomato-WPRE-SV40	UPenn Vector Core	Addgene_105554-AAV1
pENN-AAV1-CamKII(0.4)-CRE-SV40	UPenn Vector Core	Addgene_105558-AAV1
AAV1-hsyn-DIO-TVA66T-dTom-CVS-N2C (g)	Allen Brain Institute	N/A
EnvA dG CVS-N2C Histone-eGFP	Allen Brain Institute	N/A
Chemicals, peptides, and recombinant proteins		
Tetrodotoxin	Abcam	ab120055; CAS: 4368-28-9
Tetrodotoxin	Tocris	1078; CAS: 4368-28-9
D-APV	Tocris	0106; CAS: 79055-68-8
4-AP	Sigma-Aldrich	CAS:504-24-5
(+)-MK 801	Tocris	0924; CAS: 77086-22-7
DNQX disodium salt	Tocris	2312; CAS: 1312992-24-7
Picrotoxin	Tocris	1128; CAS: 124-87-8
MNI-caged-L-glutamate	Tocris	1490; CAS: 295325-62-1
OGB-6F	Invitrogen	O23990
CPP	Sigma-Aldrich	C104; CAS: 126453-07-4
Alexa 488	Invitrogen	A10436
Alexa 594	Invitrogen	A10438
DAPI	Thermo Fisher Scientific	62248
Experimental models: Organisms/strains		
C57/bl6 mice	Jackson Labs	RRID: IMSR_JAX:000664
Software and algorithms		
MATLAB (R2018a)	MathWorks	https://www.mathworks.com
ImageJ	National Institutes of Health	https://imagej.nih.gov/ij/index.html
Prism	Graphpad	RRID:SCR_002798
Other		
Dagan BVC-700A	Dagan Corporation	N/A
Electro-optical modulator	Conoptics	M350–50
Leica VT1200 S Fully automated vibrating blade microtome	Leica	VT1200 S
MaiTai DeepSee	Spectra-Physics	MAI TAI HP DS
Photosensor module	Hamamatsu	H7422A-40
Ultima *In Vitro* Multiphoton Microscope System	Bruker	N/A
Collimated LED for Olympus BX	ThorLabs	M625L4-C1

REAGENT or RESOURCE	SOURCE	IDENTIFIER
473 nm laser	OptoEngine LLC	MSL-FN-473/1~100mW
TCS SP8 upright confocal microscope	Leica	DM6000